Version of Record: https://www.sciencedirect.com/science/article/pii/S016980952200062X
Manuscript_d16a14a6b8068fdb04fd6a24a8a736fb

Changes in the ozone chemical regime over the contiguous United States inferred by the inversion of NO_x and VOC emissions using satellite observation

Jia Jung[1], Yunsoo Choi[1*], Seyedali Mousavinezhad[1], Daiwen Kang[2], Jincheol Park[1], Arman Pouyaei[1], Masoud Ghahremanloo[1], Mahmoudreza Momeni[1], and Hyuncheol Kim[3,4]

[1]Department of Earth and Atmospheric Sciences, University of Houston, TX, USA

[2]Center for Environmental Measurement and Modeling, US Environmental Protection Agency, Research Triangle Park, NC, USA

[3]Air Resources Laboratory, National Oceanic and Atmospheric Administration, College Park, MD, USA

[4]Cooperative Institute for Satellite Earth System Studies, University of Maryland, College Park, MD, USA

*Corresponding author: ychoi23@central.uh.edu

Abstract

To investigate changes in the ozone (O_3) chemical production regime over the contiguous United States (CONUS) with accurate knowledge of concentrations of its precursors, we applied an inverse modeling technique with Ozone Monitoring Instrument (OMI) tropospheric nitrogen dioxide (NO_2) and total formaldehyde (HCHO) retrieval products in the summers of 2011, 2014, and 2017, years in which United States National Emission Inventory were based. The inclusion of dynamic chemical lateral boundary conditions and lightning-induced nitric oxide emissions significantly account for the contribution of background sources in the free troposphere. Satellite-constrained nitrogen oxide (NO_x) and non-methane volatile organic compounds (NMVOCs) emissions mitigate the discrepancy between satellite and modeled columns: the inversion suggested 2.33 – 2.84 (1.07 – 1.34) times higher NO_x over the CONUS (over urban regions) and 0.28 – 0.81 times fewer NMVOCs emissions over the southeastern United States. The model-derived HCHO/NO_2 column ratio shows gradual spatial changes in the O_3 production regime near urban cores relative to previously defined threshold values representing NO_x and VOC sensitive conditions. We also found apparent shifts from the NO_x-saturated regime to the transition regime (or the transition regime to the NO_x-limited regime) over the major cities in the western United States. In contrast, rural areas, especially in the east-southeastern United States, exhibit a decreased HCHO/NO_2 column ratio by -1.30 ± 1.71 with a reduction in HCHO column primarily driven by meteorology, becoming sensitive to VOC emissions. Results show that incorporating satellite observations into numerical modeling could help policymakers implement appropriate emission control policies for O_3 pollution.

Key Words: HCHO/NO_2 factor, Inverse modeling, ozone chemical regime, OMI, CMAQ-DDM

1. Introduction

Ground-level ozone (O_3) is primarily formed through complex nonlinear photochemical reactions between nitrogen oxide (NO_x) and volatile organic compounds (VOCs) in the presence of sunlight, while stratospheric intrusion contributes a substantial amount of O_3 in the upper troposphere (Holton et al., 1995; Knowland et al., 2017). In the United States (U.S.), as long-term exposure to high-level O_3 concentrations poses substantial threats to human health and ecosystems, a number of national regulations have been implemented during the last few decades to reduce O_3 and its precursors, resulting in a substantial reduction in O_3 concentrations. For instance, the Nitrogen Oxides States Implementation Plan Call (NO_x SIP Call), enforced by the U.S. Environmental Protection Agency (EPA) from 2003 to 2004, has reduced the interstate transport of O_3, resulting in a remarkable reduction in O_3 concentrations by 20% to 30% (Foley et al., 2015). Meanwhile, the long-range transport of O_3 and its precursors (e.g., NO_x, VOCs, and carbon monoxide (CO)), especially from Asia and Europe, becomes important due to their increasing contribution to background O_3 levels in the U.S. (Jacob et al., 1999; Lee et al., 2021).

Depending on the relative availabilities of NO_x and VOCs concentrations, the O_3 formation regime is conventionally classified into three categories—NO_x-limited, transition, and NO_x-saturated (VOC-limited) —all of which determine the rate of O_3 production. The substantial reduction in O_3 precursor emissions could alter VOC/NO_x ratio, resulting in changes in the O_3 chemical regime. Previous studies have reported that the O_3 chemical regime has shifted toward the NO_x-limited regime in the U.S. urban environments in response to pronounced NO_x emission reductions in warm seasons (Jin et al., 2020, 2017). Moreover, variations in changes of different emission sectors also contribute to the spatial variations in the concentrations of O_3 precursors and the O_3 chemical regime (Jiang et al., 2018).

The identification of the O_3 chemical regime is essential to determining the effectiveness of O_3 control policies. Based on analysis of a simple trajectory model, Sillman (1995) compared reactive odd nitrogen (NO_y), $O_3/(NO_y - NO_x)$, HCHO/NO_y, and hydrogen peroxide (H_2O_2)/nitric acid (HNO_3) as indicator species of O_3-NO_x-VOC sensitivity. The following study by Tonnesen and Dennis (2000) found that the HCHO-to-NO_2 ratio (HCHO/NO_2) is more valuable than HCHO/NO_y, owing to the short lifetime of NO_2 and HCHO that can serve as proxies of NO_x and non-methane volatile organic compounds (NMVOCs) emissions. Satellite data have broader

spatial and temporal coverage than in situ observations; hence, numerous studies have employed satellite-derived HCHO/NO_2 ratio (Choi et al., 2012; Duncan et al., 2010; Martin et al., 2004; Schroeder et al., 2017). Recent studies, however, have reported that changes in satellite-observed NO_2 and HCHO columns do not necessarily reflect the trends in the U.S. National Emission Inventory (NEI) and near-surface air quality. While the decrease of the satellite-observed tropospheric NO_2 column has become slower since 2009, the trend of NEI indicates a monotonic decrease in NO_x emissions (Jiang et al., 2018; Silvern et al., 2019). Moreover, because of the significant reduction in surface emissions, the relative contribution of the background sources of NO_x in the troposphere (e.g., lightning and soils) has increased, as has its impact on atmospheric chemistry (Kang et al., 2019; Silvern et al., 2019). In the case of HCHO, its trend in urban cores is consistent with the trend of NEI emissions. However, biogenic and biomass burning (open fire) emissions, primarily driven by the temperature, are generally dominant over the southeastern and western U.S., respectively, in summer months (Curci et al., 2010; Palmer et al., 2003; Zhu et al., 2017).

Chemical transport models (CTMs) are useful for not only connecting the column and surface air quality but also identifying the response of ozone to changes in the emissions of ozone precursors. The uncertainty of emission inventories, however, has resulted from the poor classification of emission sources and the limited knowledge of NO_x and NMVOCs emission factors (Tian et al., 2010), which often cause significant bias in the results of models when they are compared to observed values. Thus, in conjunction with the broad coverage of satellite measurements, top-down emission estimation is well established and applied in a number of studies optimizing NO_x and NMVOCs emission inventories from various areas around the globe. In particular, a rich legacy of NO_2 and HCHO column retrievals observed by the National Aeronautics and Space Administration (NASA) Ozone Monitoring Instrument (OMI) has provided nearly continual daily column retrievals at a relatively high resolution since July 2004, which is suitable for long-term analysis and application. Since the public release of the data, the OMI column retrievals have been well validated (Baek et al., 2014; Herman et al., 2009; Lamsal et al., 2014; Wang et al., 2017; Zhu et al., 2016) and applied in numerous studies conducting a top-down assessment of emission inventories (Bae et al., 2020; Goldberg et al., 2019; Kaiser et al., 2018; Millet et al., 2008; Souri et al., 2020, 2016; Tang et al., 2013a; Zhu et al., 2014).

In this study, we applied an analytical inverse modeling technique with OMI NO_2 and HCHO column retrievals and estimated top-down NO_x and NMVOCs emissions over the contiguous U.S. (CONUS) in the summers of 2011, 2014, and 2017, which were the base years that the U.S. NEI was formulated. From adjusted emissions, we examined changes in the ozone chemical regime over the CONUS throughout the study period.

2. Overview of Measurements, the Modeling System, and the Inverse Modeling Method

2.1 OMI NO_2 and HCHO Column Retrievals

The Ozone Monitoring Instrument (OMI) was launched in 2004 on the NASA Earth Observing System (EOS) Aura satellite, which is in a sun-synchronous polar orbit with a local equator crossing time of 13:45 ± 0:15. OMI is a nadir-viewing near-UV/visible spectrometer that provides complete global coverage of the daily measurements of several air quality components (e.g., NO_2, sulfur dioxide (SO_2), bromine monoxide (BrO), HCHO, and aerosols) with spatial resolutions of up to 13 × 24 km^2 at the nadir, spectral range of 264 – 504 nm, and spectral resolutions between 0.42 nm and 0.64 nm (Levelt et al., 2006).

In this study, we use the tropospheric NO_2 and total HCHO columns from the OMI operational retrieval products (Level 2 and version 3) released by the NASA Goddard Earth Sciences Data and Information Service Center (GES DISC). The tropospheric NO_2 column retrievals are calculated through multiple procedures: using a spectral fitting algorithm from the normalized visible wavelength (402 – 465 nm) to retrieve the slant column, calculating the air mass factor (AMF), and separating troposphere and stratosphere column densities. Details of the data quality assurance and retrieval process are available in previous studies (Bucsela et al., 2013; Choi et al., 2020; Krotkov et al., 2017; Lamsal et al., 2014). To filter out unqualified pixels, we use pixels with a cloud fraction of less than 30%, a terrain reflectivity of less than 30%, a solar zenith angle of less than 65º, a data quality flag as zero, and a cross-track quality flag as zero to screen rows affected by row anomalies (Torres et al., 2018).

This study employed the total HCHO column retrieved by the new Smithsonian Astrophysical Observatory (SAO) algorithm (González Abad et al., 2015). Because of increased

background HCHO and noise from the previous product, the retrieval algorithm has been updated in the processing of data such as the fitting window (328.5 – 356.5nm), the AMF calculation, and the reference sector re-normalization of vertical column densities. With greatly reduced noise and increased temporal stability, the quality of the data has significantly improved (González Abad et al., 2015). In addition, the estimated detection limit is 1×10^{16} molecules cm^{-2} (González Abad et al., 2015). Similar to NO_2, we use pixels with a cloud fraction of less than 40%, a solar zenith angle of less than 65º, a data quality flag as zero, a cross-track quality flag as zero, and a vertical column density with a range of -2 to 2×10^{15} molecules cm^{-2}. For both the OMI NO_2 and HCHO columns, we recalculated the AMF and replaced the prior profile of the OMI data with the profile of the CMAQ simulation of this study.

2.2 Modeling Setup

To compute both atmospheric concentrations of gaseous and particulate pollutants and first-order sensitivity coefficients, required for conducting inverse modeling, we use the Community Multiscale Air Quality model configured with the decoupled direct method in three dimensions (CMAQ DDM-3D) based on CMAQ model version 5.2 (Cohan et al., 2005; Napelenok et al., 2006), developed and released by the EPA. Our study domain covering the CONUS utilizes 12 km grid spacing with 459 × 299 grid points (shown in Figure 1), while the vertical extent between the surface and 100 hPa is discretized with 27 layers of variable thickness. We use carbon bond (CB6r3) for the gas phase and AERO6 for the aerosol chemical mechanism. We obtained the chemical initial and boundary conditions from the CMAQ model with the in-line dust model covering the entire Northern Hemisphere (HCMAQ) (Mathur et al., 2017), providing dynamic chemical lateral boundary conditions in a consistent physical configuration. Details of the HCMAQ simulation and its emission data can be found in Jung et al. (2021) and Vukovich et al. (2018). Since the HCMAQ simulation was based on the year 2016, we applied seasonal scaling for gaseous species based on the comparison with multiple satellite datasets such as the NASA OMI/Aura vertical O_3 profile 1-Orbit level 2 data, NASA OMI tropospheric NO_2 and total HCHO level 2 version 3 data, and the Measurement of Pollution in the Troposphere (MOPITT) CO level 2 version 8 data (shown in Figure S1).

Using the Weather Research and Forecasting (WRF) model version 4.0, we estimated meteorological fields over the U.S. 12 km modeling domain (shown in Figure 1) with the initial and boundary conditions from the National Centers for Environmental Prediction (NCEP) North American Regional Reanalysis (NARR), which has a 32 km horizontal resolution and three hours of temporal resolution. Detailed configurations of both the CMAQ and WRF models can be found in Table 1. In an effort to enhance model performance in simulating meteorological fields, we applied indirect soil moisture and temperature nudging technique (Pleim and Gilliam, 2009; Pleim and Xiu, 2003) together with a four-dimensional data assimilation option every 6 hours above the planetary boundary layer (PBL) for the temperature, the water mixing ratio, and wind components with an order of magnitude of 10^{-5} (Gilliam et al., 2012; Hogrefe et al., 2015).

In this study, we conducted model simulations for the summers (June, July, and August) of 2011, 2014, and 2017. Each simulation was preceded by 10 days of model spin-up, allowing for initializing the deep soil moisture with the PX LSM.

2.3 Emission Data

The emission data for this study comprises anthropogenic, lightning-induced, biogenic, and biomass burning emissions. Previous studies have addressed the significant contribution of non-anthropogenic sources, mainly from soil and lightning, to NO_x emissions (Qu et al., 2021; Silvern et al., 2019). The absence of background NO_x emissions, however, results in the significant underestimation of NO_2 mixing ratios in the free troposphere and the misalignment of emission adjustments from the inversion. Therefore, before proceeding with inverse modeling, we must include proper non-anthropogenic background sources (Silvern et al., 2019; Tang et al., 2013b; Travis et al., 2016).

To collect the anthropogenic emissions, we use the U.S. EPA NEI 2011 v6.3, 2014 v7.1, and 2017 (Eyth et al., 2016; Eyth and Vukovich, 2016) emission inventories for each corresponding year. The Sparse Matrix Operator Kernel Emission (SMOKE) system and associated tools were used for processing NEI to prepare the CMAQ-ready emissions. Details regarding NO_x and NMVOCs emission are available in the NEI technical support documents released by the EPA.

Briefly, NO_x and NMVOCs emissions from NEI point sources comprising the commercial marine vessels, non-EGU (Electric Generating Utility) emissions, and oil and gas sectors are prepared using the State/Local/Tribal (S/L/T)-submitted emissions. NO_x emissions from the EGU sector are based on the hourly Continuous Emissions Monitoring (CEM) emissions reported to the EPA Clean Air Markets Division (CAMD) database. The EPA Motor Vehicle Emissions Simulator (MOVES) model estimates daily emissions for NO_x and calculates fuel consumption for the on-road sector based on S/L/T-submitted activity data. The MOVES also uses ratios from some primary emissions to calculate emissions for NMVOCs. Except for rail, shipping lanes (for coastal counties), and ports, which are more finely resolved to the county level, the NO_x and NMVOCs emissions for stationary sectors, including non-point oil and gas, residential wood combustion, non-road, and other non-point are generated at the county level. The shipping lane emissions outside of 200 nautical miles from the U.S. coastline were filed in from non-NEI sources.

To compute biogenic emissions, we use the Biogenic Emission Inventory System (BEIS) version 3.61, which is built within the SMOKE, estimating hourly emissions of the biological activity of vegetative species and microbial activity from soils such as nitric oxide (NO), CO, and VOCs (e.g., isoprene, terpene, and sesquiterpene) with several meteorological variables (e.g., leaf area index, surface pressure, 2-m mixing ratio, precipitation, solar radiation, and soil properties). The use of PX LSM with indirect soil moisture and temperature nudging reduces bias in the 2 m air temperature and the 2 m water vapor mixing ratio used to calculate soil NO emission (Pleim and Gilliam, 2009; Pleim and Xiu, 2003).

We calculate lightning-induced NO emissions by the in-line lightning NO (LNO) production module implemented in the CMAQ. Estimates of the LNO emissions are based on hourly flash rates from the National Lightning Detection Network (NLDN) (Orville, 2008). A detailed description of the lightning NO production scheme can be found in (Allen et al., 2012; Kang et al., 2019). The contribution of LNO to the total NO_x emissions ranges 16% and 20% over the Rocky Mountains area and the southeastern region of the U.S. for the summer of 2011 (Kang and Pickering, 2018) and 30% over the mountainous western states in July 2011 (Kang et al., 2020), affecting O_3 concentrations in the upper troposphere and the surface as well as the deposition of nitrogen (Allen et al., 2012; Kang et al., 2020, 2019; Kang and Pickering, 2018).

For biomass burning emissions, we refer to the Fire Inventory from National Center for Atmospheric Research (FINN) version 1.5, which provides daily global estimates of trace gas and particulate matter emissions based on observation by the Moderate Resolution Imaging Spectroradiometer (MODIS) (Wiedinmyer et al., 2014, 2011, 2006). In this study, the gridded open fire emissions from the FINN are vertically distributed in the PBL (65%) and upper atmosphere (35%).

2.4 Inverse Modeling of NO_x and NMVOCs Emissions

Given the relatively short lifetime of NO_2 and HCHO, their satellite columns often correlate with NO_x and NMVOCs emissions and can be applied to estimations of top-down emission inventories. We proceed the inverse modeling for total NO_x and NMVOCs emissions after combining anthropogenic, biogenic, and biomass burning emissions. To constrain bottom-up emissions of total NO_x and NMVOCs, we apply the Gauss-Newton method, an analytical inversion approach to finding solutions to problems that are not rigorously nonlinear, described in Rodgers (2000). This approach assumes no correlation between observations and emission errors, and the error covariances of observations and emissions with zero bias Gaussian probability density functions. The inversions with the Newtonian iterations gradually approach convergence at the zero of the gradients of the cost function, shown in Eq. (1). Posteriori emissions can be estimated by Eq. (2).

$$J(x) = \frac{1}{2}\big(y - F(x)\big)^T S_o^{-1}\big(y - F(x)\big) + \frac{1}{2}(x - x_a)^T S_e^{-1}(x - x_a) \quad (1)$$

$$x_{i+1} = x_a + S_e K_i^T (K_i S_e K_i^T + S_o)^{-1}[y - F(x_i) + K_i(x_i - x_a)] \quad (2)$$

where x and x_a represent a posteriori and a priori emissions, respectively. The observational error covariances (S_o) for the OMI NO_2 and HCHO are based on column uncertainties provided in the OMI dataset in conjunction with uncertainties validated by previous studies (González Abad et al., 2015; Lamsal et al., 2014). To find the error covariance of emission (S_e), we calculate the total error covariance by combining all sector emissions (NO_x/NMVOCs) from anthropogenic (50%/150%), biogenic (200%/200%), and biomass burning (100%/300%) sources. We note that we considered NMVOCs species having relatively shorter lifetimes, such as HCHO, ethene, acetaldehyde, isoprene, ethanol, and acetone. This study applies the CMAQ

DDM-3D model to correlate the columns of NO_2 and HCHO with their emissions (F) (first-order sensitivity) in order to calculate the Jacobian matrix (K).

3 Results

3.1 Changes in the NO_2 and HCHO Column Retrievals and the Contribution of Background Sources to the Upper Troposphere

Figure 2 illustrates the spatial distribution of seasonally averaged tropospheric NO_2 and total HCHO vertical column densities from the OMI for the summers (June to August) of 2011, 2014, and 2017 over the CONUS. The AMFs of both columns were adjusted based on the NO_2 and HCHO columns simulated in this study. The OMI tropospheric NO_2 columns showed large values in cities with high population density and industrial activity, such as Seattle, Los Angeles, Houston, Chicago, and New York. During the study period, the NO_2 columns exhibited a similar spatial distribution, but with a domain-wide decrease by -6.10% and -7.95% in 2014 and 2017, respectively, with respect to 2011. With regard to HCHO columns, high values were predominant in the southeastern U.S., mainly resulting from oxidation of biogenically emitted isoprene (Palmer et al., 2003; Zhu et al., 2017). In this region, HCHO columns consistently declined by -26.16% in 2014 and -33.68% in 2017 compared to those in 2011, while more widespread high values were found over the western area.

The variability of satellite-observed NO_2 and HCHO columns reflects changes in bottom-up emissions and the contribution of background sources in the upper troposphere (Silvern et al., 2019). In Figure 3, we plotted seasonal averaged changes in observed and simulated tropospheric NO_2 and total HCHO column densities in four regions: domain-wide (i.e., CONUS), urban and rural regions, and southeastern (SE) areas. We defined an urban area based on the U.S. census-based surrogate, where population density is at least 1,000 people per square mile, denoted in red in Figure 1; and we defined a rural region, designated by gray in Figure 1, as more than 20 km away from both urban regions and power plants with a capacity of 1 MW or more, based on the U.S. Energy Information Administration. The southeastern (SE) area (a blue rectangle shown in Figure 1) denotes an area with dominant lightning-induced (to the total NO_x emissions) and biogenic emissions (to the total NMVOCs emissions) over the CONUS. In SE,

NMVOCs emissions from biogenic sources are dominant, so we excluded the SE area when we analyzed modeled and observed HCHO columns over urban and rural regions in Figure 3.

Also shown in Figure 3 are modeled NO_2 and HCHO columns with three different background setups that show the contribution of background sources to the upper troposphere: those with dynamic lateral boundary conditions and LNO emissions, those with dynamic lateral boundary conditions and no LNO emissions, and those with profile (static) lateral boundary conditions and no LNO emissions. We note that we weighted the contributions from lightning and the transport of air pollution for the background sources in the upper troposphere, while we included open fire and soil emissions in prior emissions, as addressed in Section 2.3. Also, surface meteorological variables (e.g., solar radiation, air temperature, and wind fields) vary concentrations of NO_2 and HCHO by altering photolysis rates, lifetime, and dispersion (Goldberg et al., 2020), as well as rates of biogenic isoprene emissions (Guenther et al., 2012). Therefore, the model performance of the meteorological variable simulation is critically linked to the reliability of both concentrations of air pollutants and the estimates of top-down emissions. We evaluated modeled hourly air temperatures and wind fields against the U.S. EPA Air Quality System (AQS) measurements over the CONUS, listed in Table 2. We found that our model and the observations were comparable, showing a strong correspondence (air temperature: IOA > 0.89, wind fields: IOA > 0.61).

The OMI NO_2 columns showed marginal changes over the CONUS during the study period; the change in urban regions, however, exhibited a decrease throughout the 2011 – 2017 period, which indicates the continuous efforts to reduce NO_x emissions. The NO_2 column in the urban and SE regions decreased by -20.83% and -16.53%, respectively, while almost steady columns were found in the rural regions throughout the study period, possibly related to the increasing contribution of non-anthropogenic sources (e.g., soil and lightning) that compensated for the reduction in anthropogenic emissions (Li and Wang, 2019; Silvern et al., 2019). Although the model simulated a general decreasing tendency of the NO_2 column, it showed a sustained underestimation compared to the OMI observations over the CONUS by 6.24×10^{14} – 1.37×10^{15} molecules cm^{-2} (11.58 – 62.78%) in the case of prior emissions and profile lateral boundary conditions. We found that the addition of dynamic lateral boundary conditions and the LNO emissions greatly reduced bias by 0.11 – 26.58%, resulting in stronger agreement with

observations, dominantly in both rural regions (16.12 – 18.07%) and SE regions (4.65 – 10.54%), primarily benefited from LNO emissions.

The OMI HCHO columns showed a steady decrease, except for the rural regions (which decreased by 5.87% in 2014 and increased by 2.75% in 2017 with respect to 2011). Since meteorology, especially temperature, drives most of the variability of HCHO columns over the CONUS (Zhu et al., 2017), a significant decline in air temperature (shown in figure S2), along with the reduction in NEI emissions, might cause a substantial decrease over the SE regions, where biogenic sources are dominant. Overall, the CMAQ model overestimated HCHO columns by up to 2.64×10^{15} molecules cm^{-2} (56.79%) compared to the OMI observations, and dynamic lateral boundary conditions amplified this overestimation (0.75×10^{15} – 3.58×10^{15} molecules cm^{-2} (5.30 – 67.60%)). In addition, the discrepancy between the OMI HCHO columns and the modeled columns were significantly large over the rural regions, which might be attributable to instrumental noise of the column retrieval, or rather the high uncertainty of the bottom-up emission inventory, particularly involving open fire emissions (e.g., injection height, the fraction of burned areas, classifications of land use and land cover, and unresolved small fires by satellites) (Hawbaker et al., 2008; Jeon et al., 2018; Mehmood et al., 2020; Shen et al., 2019; Souri et al., 2017; Wiedinmyer et al., 2011).

When compared with NO_2 and O_3 concentrations measured by P-3B aircraft during the NASA DISCOVER-AQ 2011 and 2014 campaigns, which took place over the Baltimore/Washington D.C. metropolitan area and northern Colorado, shown in Figure 4 (flight tracks, flight time, and altitude were shown in Figure S3), the base model tended to under-predict both NO_2 and O_3 concentrations in the upper troposphere, as reported in Napelenok et al. (2008), possibly owing to lack of emission sources and a chemical lifetime of NO_2. Promisingly, the model performance greatly improved in the upper troposphere (above 2.5 km) with the dynamic lateral boundary conditions (as much as 23.24% for NO_2 and 14.76% for O_3) and LNO emissions (as much as 9.33% for NO_2 and 26.34% for O_3). An enhancement of model performance in the upper troposphere was also found by comparison with ozonesonde measurements, displayed in Figure S4. The electrochemical concentration cell (ECC) attached to ozonesonde provides simultaneous measurements of ozone and meteorological quantities until the balloon bursts about at altitudes of 35 km (Tarasick et al., 2021). Improvements in the model results suggest the need

to account for background sources in the free troposphere, which would prevent the misalignment of emission adjustments, discussed in the following section.

3.2 Top-Down Estimation of NO_x and NMVOCs Emissions

Before investigating changes in the ozone chemical production regime, we adjusted total NO_x and NMVOCs emissions with the OMI NO_2 and HCHO column retrievals found by the inverse modeling approaches that we addressed in Section 2.4 in order to acquire accurate knowledge of the concentrations of ozone precursors. It is worth noting that we assumed the uncertainty of bottom-up emissions as the main contributor to the discrepancy between modeled (with prior emissions, dynamic boundary conditions, and LNO emissions) and satellite-observed columns; the discrepancy, however, could also be explained by several other deficiencies in chemical processes (e.g., a lifetime of alkyl nitrate) and meteorology (e.g., wind fields).

Figures 5 and 6 display the spatial distribution of averaged tropospheric NO_2 and total HCHO column densities simulated with prior and posterior emissions corresponding to the OMI observations (shown in Figure 2) and their differences with respect to the column with prior emissions. For both the NO_2 and HCHO columns, the modeled columns with posterior emissions more closely agreed with those from the OMI observations. In most areas, the modeled tropospheric NO_2 column, compared to that of the OMI observations, exhibited an underestimation throughout the study period (Figures 2 and 5), but using posterior emission (shown in Figure S5), we observed a large reduction in bias, increasing the NO_2 column by as much as 21.55 ± 28.76% nationwide. The adjustment ratio between the prior and posterior NO_x emissions was slightly high in 2017 (2.84 ± 1.99) than in 2011 (2.33 ± 1.83) and 2014 (2.62 ± 2.19) over the CONUS (Figure S8), predominantly in the central and western regions, shown in Figure S5. The absolute amount of NO_x emissions is much smaller over rural regions compared to urban regions, possibly resulting in an excessive emission adjustment ratio over the CONUS. As shown in Figure S8, the posterior NO_x emissions are 7 – 34% higher than that of prior emissions over urban regions. We also found increased NO_x emissions and NO_2 columns in Mexico and Canada, which in turn potentially enhanced the influence of O_3 precursors transported from outside of the CONUS. With regard to HCHO, the model with prior emissions overestimated the total HCHO column over the southeastern U.S. by 6.77 – 14.85%. The

inversion suggested 0.81 ± 0.30 times fewer NMVOCs emissions over the region in 2011, and the adjustment ratio decreased as 0.63 ± 0.28 in 2014 and 0.59 ± 0.24 in 2017, respectively (Figure S8). In addition, we observed enhancement of the HCHO column over the northwestern U.S. with posterior emissions, possibly related to open fire events; the magnitude, however, was relatively small (Figure S6).

To validate the model output with prior and posterior emissions, we compared the AQS measurements to modeled surface daytime (12 – 17 LST) averaged NO_2 and maximum daily 8-hour average (MDA8) O_3 concentrations over the CONUS, shown in Figure S9. As the number of AQS sites for each year varied throughout the study period, we used measurement data from monitoring sites (230 sites for NO_2 and 1,023 sites for O_3) with more than 50% of temporal coverage to ensure both data quality and consistency. Following Lamsal et al. (2008), we also corrected NO_2 measurements for the AQS sites to remove any interferences from several reactive oxidized nitrogen-containing species (e.g., alkyl nitrate, peroxyacetyl nitrate (PAN), and nitric acid (HNO_3)) based on the modeled output. The performance of the model with the posterior emissions was superior, with a significantly reduced bias of 38 – 96% for NO_2. However, posterior emissions, unfortunately, enhanced the tendency of the general model to overestimate O_3 concentrations, frequently reported in previous studies (Hogrefe et al., 2018; Kitayama et al., 2019; Travis et al., 2016). More precisely, we compared model performance at the percentile of O_3 distribution in Figure S10. The model with the posterior emissions amplified the overestimation of ozone at the lower percentile (< 60%), where the majority of ozone data was presented. On the contrary, underestimation of ozone at a higher percentile (> 60%) slightly reduced with the posterior emission in 2011; however, model bias increased in 2014 and 2017. These results indicate that adjustments to the emissions of O_3 precursors cannot fully address the total uncertainty of the model, and the bias is associated more with systematic problems in the model that modulate surface O_3 such as vertical mixing highly related to meteorological factors (e.g., heat flux), as well as deficient ozone deposition in the boundary layer (Hogrefe et al., 2018; Travis et al., 2016).

3.3 Changes in the Ozone Chemical Regime over the CONUS

The $HCHO/NO_2$ ratio as an indicator of the ozone chemical regime is highly dependent on meteorological and photochemical conditions, as well as characteristics of satellite retrievals and CTMs, resulting in a wide range of values. For instance, Martin et al. (2004) proposed the $HCHO/NO_2$ ratio of 1 for defining NO_x-saturated (< 1) and NO_x-limited (> 1) regimes. Choi et al. (2012) and Duncan et al. (2010) used the ratios of 1 and 2 to categorize the ozone chemical regime into NO_x-saturated (< 1), NO_x-limited (> 2), and transition ($1 < HCHO/NO_2 < 2$) regimes. Chang et al. (2016) found different threshold values of ozone chemical regime with OMI (1.5 and 2.3) and Global Ozone Monitoring Experiment-2 (GOME-2) (1 and 1.85). Ozone production sensitivity to the $HCHO/NO_2$ ratio derived by CTMs could vary depending upon the study domain, chemical mechanism, and meteorological conditions (Chang et al., 2016; Jin et al., 2017). To avoid the misclassification of the ozone chemical regime, we conducted an experiment to define threshold values by using the CMAQ model with posterior emission inventory based on the year 2011. Figure 7 (a) represents the difference of averaged surface O_3 concentrations between the baseline CMAQ model and the CMAQ with perturbed emission (20% reductions in NO_x and NMVOCs emissions) along with the corresponding modeled $HCHO/NO_2$ column ratio for the revisit time of the OMI satellite (13:00 – 14:00 LST) since we adjusted emissions of ozone precursors based on OMI column retrievals. In addition, the revisit time of the OMI satellite is beneficial to analyze the ozone chemical regime when the ozone production is maximum in a day in conjunction with the smallest solar zenith angle and most profound boundary layer height (Jin et al., 2017). To clearly examine the difference of O_3 with perturbed emission, we considered model grids over polluted regions where the modeled tropospheric NO_2 column is greater than 1×10^{15} molecules cm^{-2} (Boersma et al., 2016; Choi et al., 2012; Schaub et al., 2006). As a response to NO_x emission reduction, surface O_3 concentrations generally increased proportionally to the $HCHO/NO_2$ ratio. The increase was dominant for a high $HCHO/NO_2$ ratio. The change in surface ozone concentrations became moderate for the case of NMVOCs emission reduction (red color); still, noticeable changes in ozone concentration were found for a low $HCHO/NO_2$ ratio.

In order to ascertain threshold values of the chemical regime, we plotted the cumulative probabilities of NO_x-limited and NO_x-saturated conditions with respect to $HCHO/NO_2$ column ratio by following Jin et al. (2017) as shown in Figure 7(b). A more detailed description of the cumulative probabilities and defining the cut-off values can be found in Jin et al. (2017). Briefly,

the NO_x-saturated condition represents the model grids where surface O_3 concentrations decrease with a 20% reduction of NO_x emissions. The NO_x-limited condition is defined in the model grids where the increase of O_3 concentrations with a 20% reduction of NO_x emissions is greater than that with a 20% reduction of NMVOCs emissions. The cumulative probability for NO_x-saturated (NO_x-limited) condition indicates the proportion of model grids that belong to the condition and have the $HCHO/NO_2$ ratio less (greater) than a given value. As with Figure 7 (a), both of the cumulative probabilities were estimated only for the revisit time of the OMI satellite (13:00 – 14:00 LST), and we excluded model grids having the modeled tropospheric NO_2 column less than 1×10^{15} molecules cm^{-2}. The threshold values for NO_x-limited and NO_x-saturated regimes are estimated as those corresponding to the 95% of cumulative probability. Accordingly, in this study, $HCHO/NO_2$ ratios of 1.6 and 2.6 are determined as the regime thresholds. Thus, $HCHO/NO_2$ ratios lower than 1.6 represent the NO_x-saturated regime, ratios greater than 2.6 represent NO_x-limited regime, while those in-between ($1.6 < HCHO/NO_2 < 2.6$) defined the transition regime.

Figure 8 (a) shows the spatial distribution of the ozone chemical production regime (based on the averaged $HCHO/NO_2$ ratio) over the CONUS in the summer of 2011, while the results for 2014 and 2017 are plotted in Figure S11. The entire CONUS is divided into three regimes according to the threshold values we defined earlier; model grids with NO_2 column density less than 1×10^{15} molecules cm^{-2} are not considered and are denoted by the gray color. Several metropolitan cities were categorized as NO_x-saturated and transition regimes, whereas the remaining rural areas were classified as NO_x-limited regimes due to the nature of urban conditions with highly concentrated traffic density and amount of vehicle emissions. According to Figure 8(b), showing the difference of $HCHO/NO_2$ ratio between 2011 and 2017, the column ratio in rural areas decreased by -1.30 ± 1.71, mostly over the eastern and southeastern U.S. This regime modification toward the NO_x-saturated condition could be explained by the increased NO_x emissions over the northeastern U.S. (Figure S7), as well as the sustained decrease of the HCHO column (Figure 3 (h-2)) as a response to meteorological change (Figure S2).

To examine the changes in the ozone chemical regime over major metropolitan cities more closely, we plotted the spatial distribution of the ozone production regime zoomed in over 5 boxes (Box A to Box E, denoted in Figure 8) in Figure 9, showing details of the selected

metropolitan areas surrounding Seattle/Portland, Los Angeles/San Francisco, Dallas/Houston, Chicago, and Detroit/Pittsburgh/New York for the summers of 2011, 2014, and 2017. In addition, Figure 10 shows changes in HCHO/NO_2 ratio at urban cores for the major 12 cities over the CONUS. The change of the ozone production regime varied during the study period. As a response to the reduction of NO_2 columns in urban regions, which was greater than that of HCHO columns (Figure S8), the clear shifts of the ozone chemical regime from NO_x-saturated to transition, or transition to NO_x-limited were found partially over metropolitan areas (e.g., Seattle, Houston, and Pittsburgh) or completely even at urban cores (e.g., Houston, San Francisco, and Salt Lake City), especially from 2014 to 2017. By contrast, Los Angeles, New York, and Portland were the cities steadily remaining in the NO_x-saturated regime throughout the study period. Also, we observed the sudden expansions of NO_x-saturated conditions at the urban cores of Houston (in 2014) and Detroit (in 2017). In general, most cities in the eastern U.S., except Pittsburgh, tended to stay in the same regime to which they were in 2011 or even came back to the NO_x-saturated regime compared to the cities in the western U.S. Many recent studies have reported the changes in ozone chemical regime over the major U.S. metropolitan areas toward NO_x-limited regime in general, but with a narrow range in the reported year when the regime change occurred, and cities still remained in NO_x-limited condition, which is related to the dataset, study period, and methodology of each study; Chang et al. (2016) showed that ozone formation in Boston, Pittsburgh, Philadelphia, and Washington has changed to NO_x-limited or transition regimes in 2007 - 2014, while New York City mostly stayed in the transition regime (2007 – 2009) and VOC-limited regime (2007 – 2009 and 2014). Jin et al. (2020) addressed that NO_x-saturated condition is occurring only in Los Angeles, Chicago, and New York City by 2013 – 2016, and Koplitz et al. (2021) showed regime change toward NO_x-limited condition over most of the U.S., and a few cities such as New York City, Chicago, Minneapolis, San Francisco, and Los Angeles are still remained in NO_x-saturated regime as in 2016.

4. Conclusion and Discussion

In this study, we examined changes in the ozone chemical regime over the CONUS in the summers of 2011, 2014, and 2017, years in which U.S. NEI data were based. To combine the benefits of both satellite retrievals and CTMs, we employed an inverse modeling technique with

OMI tropospheric NO_2 and total HCHO column retrievals to estimate NO_x and NMVOCs emissions. To avoid misalignment of the emission adjustment, we applied dynamic chemical lateral boundary conditions and lightning-induced nitric oxide emissions, resulting in better representation of NO_2 and O_3 concentration in the upper atmosphere, confirmed by comparisons with measurements from the DISCOVER-AQ campaigns and two ozonesonde sites.

Compared to OMI observations, the model with the top-down estimated NO_x and NMVOCs emissions showed remarkably better performance for simulating tropospheric NO_2 and total HCHO columns and alleviated the nationwide underestimation of the NO_2 column and the overestimation of the HCHO column appearing over the southeastern U.S. We then used the CMAQ model to determine the threshold values of the ozone production regime, which closely represented the ozone chemical conditions of this study: NO_x-saturated ($HCHO/NO_2 < 1.6$), a transition ($1.6 < HCHO/NO_2 < 2.6$), and NO_x-limited ($HCHO/NO_2 > 2.6$), which is slightly distinct from other studies by Chang et al. (2016), Choi et al. (2012), Duncan et al. (2010) and Jin et al. (2017). This is because the threshold value of the $HCHO/NO_2$ ratio represents the unique ozone chemistry of the CTM depending upon several influencing factors such as study domain, chemical mechanism, and meteorological condition; therefore, the applicability of the threshold value in other studies under different conditions is a subject of further investigation. During the study period, many of the major metropolitan areas over the CONUS, classified as NO_x-saturated conditions in the year 2011, showed a clear shift toward a NO_x-limited condition followed by a greater reduction in the NO_2 column than that in the HCHO column. A few of the cities, mostly located in the eastern U.S., did not show a significant change in their ozone chemical regimes. Interestingly, we found that despite the substantial reduction in the NO_2 columns, changes in meteorological conditions such as air temperature and precipitation exhibited a decrease in the HCHO column over the southeastern U.S. As a result, the ozone regime over the region slightly moved toward a NO_x-saturated condition.

In spite of our best efforts to gain accurate knowledge of the emissions of ozone precursors, we observed an amplified overestimation of modeled ozone concentrations at the surface. This finding indicates systematic model bias stemming from uncertainty in chemical and physical processes, which lies beyond the scope of this study. Also, the inverse modeling method we

applied in this study does not fully address the effect of transport, which could be mitigated by applying more advanced approaches such as the four-dimensional variational (4D-Var) method.

This study showed remarkable spatial and temporal variation of the ozone chemical regime over the CONUS. As a result of continuous efforts devoted to decreasing anthropogenic emissions and rapid climate change, the ozone chemical regime could vary more frequently, which might require further adjustments in current ozone control policies. Thus, armed with a better knowledge of ozone precursors and ozone chemical conditions, those charged with implementing appropriate emission control policies in a timely matter could benefit from the approach used in this study.

Acknowledgments: This study was supported by NASA's Aura Science Team Grant (NNH19ZDA001N-AURAST). We are grateful for the support of the Research Computing Data Core at the University of Houston for assistance with the calculations carried out in this work.

Data Availability Statement: The OMI/Aura Level 2 tropospheric NO_2 and total HCHO column data products are available from the NASA Goddard Earth Science (GES) Data and Information Services Center (DISC) (https://disc.gsfc.nasa.gov/datasets/OMNO2_003/summary?keywords=no2, https://disc.gsfc.nasa.gov/datasets/OMHCHO_003/summary?keywords=hcho). The NCEP NARR data can be downloaded from https://rda.ucar.edu/datasets/ds608.0/. The FINN data can be acquired from https://www.acom.ucar.edu/Data/fire. The lightning flash data are available for purchase from Vaisala Inc. (https://www.vaisala.com/en/products/systems/lightning-detection). For this study, the native form of the lightning flash data was provided by Dr. Hyuncheol Kim at the NOAA, and processed into the required format of the CMAQ model with the considerable assistance of Dr. Daiwen Kang at the EPA. The EPA AQS data (pre-generated) for meteorology and air quality measurement over the U.S. is available from https://aqs.epa.gov/aqsweb/airdata/download_files.html. Aircraft measurement during the DISCOVER-AQ 2011 (Baltimore-Washington, D.C.) and 2014 (Colorado) campaigns were

distributed by NASA (https://www-air.larc.nasa.gov/missions/discover-aq/discover-aq.html). Ozonesonde data is downloaded from the NOAA Global Monitoring Laboratory/Earth System Research Laboratories (https://gml.noaa.gov/dv/data/index.php?category=Ozone&type=Balloon). The model outputs from the primary simulations can be downloaded from https://doi.org/10.5281/zenodo.5590569.

Disclaimer: This paper has been subjected to an EPA review and approved for publication. The views expressed here are those of the authors and do not necessarily reflect the views or policies of the U.S. Environmental Protection Agency (EPA).

References:

Alapaty, K., Herwehe, J.A., Otte, T.L., Nolte, C.G., Bullock, O.R., Mallard, M.S., Kain, J.S., Dudhia, J., 2012. Introducing subgrid-scale cloud feedbacks to radiation for regional meteorological and climate modeling. Geophysical Research Letters 39. https://doi.org/10.1029/2012GL054031

Allen, D.J., Pickering, K.E., Pinder, R.W., Henderson, B.H., Appel, K.W., Prados, A., 2012. Impact of lightning-NO on eastern United States photochemistry during the summer of 2006 as determined using the CMAQ model. Atmospheric Chemistry and Physics 12, 1737–1758. https://doi.org/10.5194/acp-12-1737-2012

Bae, C., Kim, H.C., Kim, B.-U., Kim, S., 2020. Surface ozone response to satellite-constrained NOx emission adjustments and its implications. Environmental Pollution 258, 113469. https://doi.org/10.1016/j.envpol.2019.113469

Baek, K.H., Kim, J.H., Park, R.J., Chance, K., Kurosu, T.P., 2014. Validation of OMI HCHO data and its analysis over Asia. Science of The Total Environment 490, 93–105. https://doi.org/10.1016/j.scitotenv.2014.04.108

Boersma, K.F., Vinken, G.C.M., Eskes, H.J., 2016. Representativeness errors in comparing chemistry transport and chemistry climate models with satellite UV–Vis tropospheric column retrievals. Geosci. Model Dev. 9, 875–898. https://doi.org/10.5194/gmd-9-875-2016

Bucsela, E.J., Krotkov, N.A., Celarier, E.A., Lamsal, L.N., Swartz, W.H., Bhartia, P.K., Boersma, K.F., Veefkind, J.P., Gleason, J.F., Pickering, K.E., 2013. A new stratospheric and tropospheric NO2 retrieval algorithm for nadir-viewing satellite instruments: applications to OMI. Atmospheric Measurement Techniques 6, 2607–2626. https://doi.org/10.5194/amt-6-2607-2013

Chang, C.-Y., Faust, E., Hou, X., Lee, P., Kim, H.C., Hedquist, B.C., Liao, K.-J., 2016. Investigating ambient ozone formation regimes in neighboring cities of shale plays in the Northeast United States using photochemical modeling and satellite retrievals. Atmospheric Environment 142, 152–170. https://doi.org/10.1016/j.atmosenv.2016.06.058

Choi, S., Lamsal, L.N., Follette-Cook, M., Joiner, J., Krotkov, N.A., Swartz, W.H., Pickering, K.E., Loughner, C.P., Appel, W., Pfister, G., Saide, P.E., Cohen, R.C., Weinheimer, A.J., Herman, J.R., 2020. Assessment of NO2 observations during DISCOVER-AQ and KORUS-AQ field campaigns. Atmospheric Measurement Techniques 13, 2523–2546. https://doi.org/10.5194/amt-13-2523-2020

Choi, Y., Kim, H., Tong, D., Lee, P., 2012. Summertime weekly cycles of observed and modeled NOx and O3 concentrations as a function of satellite-derived ozone production sensitivity and land use types over the Continental United States. Atmospheric Chemistry and Physics 12, 6291–6307. https://doi.org/10.5194/acp-12-6291-2012

Cohan, D.S., Hakami, A., Hu, Y., Russell, A.G., 2005. Nonlinear Response of Ozone to Emissions: Source Apportionment and Sensitivity Analysis. Environmental Science & Technology 39, 6739–6748. https://doi.org/10.1021/es048664m

Curci, G., Palmer, P.I., Kurosu, T.P., Chance, K., Visconti, G., 2010. Estimating European volatile organic compound emissions using satellite observations of formaldehyde from the Ozone Monitoring Instrument. Atmospheric Chemistry and Physics 10, 11501–11517. https://doi.org/10.5194/acp-10-11501-2010

Duncan, B.N., Yoshida, Y., Olson, J.R., Sillman, S., Martin, R.V., Lamsal, L., Hu, Y., Pickering, K.E., Retscher, C., Allen, D.J., Crawford, J.H., 2010. Application of OMI observations to a space-based indicator of NOx and VOC controls on surface ozone formation. Atmospheric Environment 44, 2213–2223. https://doi.org/10.1016/j.atmosenv.2010.03.010

596 Eyth, A., Vukovich, J., 2016. Technical Support Document (TSD) preparation of emissions inventories for
597 the version 6.3, 2011 emissions modeling platform. US Environmental Protection Agency, Office
598 of Air Quality Planning and Standards.
599 Eyth, A., Vukovich, J., Farkas, C., Strum, M., 2016. Technical Support Document (TSD): Preparation of
600 Emissions Inventories for the Version 7.1 - 2016 North American Emissions Modeling Platform.
601 Foley, K.M., Hogrefe, C., Pouliot, G., Possiel, N., Roselle, S.J., Simon, H., Timin, B., 2015. Dynamic
602 evaluation of CMAQ part I: Separating the effects of changing emissions and changing
603 meteorology on ozone levels between 2002 and 2005 in the eastern US. Atmospheric
604 Environment 103, 247–255. https://doi.org/10.1016/j.atmosenv.2014.12.038
605 Gilliam, R.C., Godowitch, J.M., Rao, S.T., 2012. Improving the horizontal transport in the lower
606 troposphere with four dimensional data assimilation. Atmospheric Environment 53, 186–201.
607 https://doi.org/10.1016/j.atmosenv.2011.10.064
608 Goldberg, D.L., Anenberg, S.C., Griffin, D., McLinden, C.A., Lu, Z., Streets, D.G., 2020. Disentangling the
609 Impact of the COVID-19 Lockdowns on Urban NO2 From Natural Variability. Geophysical
610 Research Letters 47. https://doi.org/10.1029/2020GL089269
611 Goldberg, D.L., Saide, P.E., Lamsal, L.N., de Foy, B., Lu, Z., Woo, J.-H., Kim, Y., Kim, J., Gao, M.,
612 Carmichael, G., Streets, D.G., 2019. A top-down assessment using OMI NO2 suggests an
613 underestimate in the NOx emissions inventory in Seoul, South Korea, during KORUS-AQ.
614 Atmospheric Chemistry and Physics 19, 1801–1818. https://doi.org/10.5194/acp-19-1801-2019
615 González Abad, G., Liu, X., Chance, K., Wang, H., Kurosu, T.P., Suleiman, R., 2015. Updated Smithsonian
616 Astrophysical Observatory Ozone Monitoring Instrument (SAO OMI) formaldehyde retrieval.
617 Atmospheric Measurement Techniques 8, 19–32. https://doi.org/10.5194/amt-8-19-2015
618 Guenther, A.B., Jiang, X., Heald, C.L., Sakulyanontvittaya, T., Duhl, T., Emmons, L.K., Wang, X., 2012. The
619 Model of Emissions of Gases and Aerosols from Nature version 2.1 (MEGAN2.1): an extended
620 and updated framework for modeling biogenic emissions. Geoscientific Model Development 5,
621 1471–1492. https://doi.org/10.5194/gmd-5-1471-2012
622 Hawbaker, T.J., Radeloff, V.C., Syphard, A.D., Zhu, Z., Stewart, S.I., 2008. Detection rates of the MODIS
623 active fire product in the United States. Remote Sensing of Environment 112, 2656–2664.
624 https://doi.org/10.1016/j.rse.2007.12.008
625 Herman, J., Cede, A., Spinei, E., Mount, G., Tzortziou, M., Abuhassan, N., 2009. NO_2 column amounts
626 from ground-based Pandora and MFDOAS spectrometers using the direct-sun DOAS technique:
627 Intercomparisons and application to OMI validation. Journal of Geophysical Research 114.
628 https://doi.org/10.1029/2009JD011848
629 Herwehe, J.A., Alapaty, K., Spero, T.L., Nolte, C.G., 2014. Increasing the credibility of regional climate
630 simulations by introducing subgrid-scale cloud-radiation interactions: RCM sims with Cu-
631 radiation interactions. Journal of Geophysical Research: Atmospheres 119, 5317–5330.
632 https://doi.org/10.1002/2014JD021504
633 Hogrefe, C., Liu, P., Pouliot, G., Mathur, R., Roselle, S., Flemming, J., Lin, M., Park, R.J., 2018. Impacts of
634 different characterizations of large-scale background on simulated regional-scale ozone over the
635 continental United States. Atmos. Chem. Phys. 18, 3839–3864. https://doi.org/10.5194/acp-18-
636 3839-2018
637 Hogrefe, C., Pouliot, G., Wong, D., Torian, A., Roselle, S., Pleim, J., Mathur, R., 2015. Annual application
638 and evaluation of the online coupled WRF–CMAQ system over North America under AQMEII
639 phase 2. Atmospheric Environment 115, 683–694.
640 https://doi.org/10.1016/j.atmosenv.2014.12.034
641 Holton, J.R., Haynes, P.H., McIntyre, M.E., Douglass, A.R., Rood, R.B., Pfister, L., 1995. Stratosphere-
642 troposphere exchange. Reviews of Geophysics 33, 403. https://doi.org/10.1029/95RG02097

Jacob, D.J., Logan, J.A., Murti, P.P., 1999. Effect of rising Asian emissions on surface ozone in the United States. Geophys. Res. Lett. 26, 2175–2178. https://doi.org/10.1029/1999GL900450

Jeon, W., Choi, Y., Souri, A.H., Roy, A., Diao, L., Pan, S., Lee, H.W., Lee, S.-H., 2018. Identification of chemical fingerprints in long-range transport of burning induced upper tropospheric ozone from Colorado to the North Atlantic Ocean. Science of The Total Environment 613–614, 820–828. https://doi.org/10.1016/j.scitotenv.2017.09.177

Jiang, Z., McDonald, B.C., Worden, H., Worden, J.R., Miyazaki, K., Qu, Z., Henze, D.K., Jones, D.B.A., Arellano, A.F., Fischer, E.V., Zhu, L., Boersma, K.F., 2018. Unexpected slowdown of US pollutant emission reduction in the past decade. Proceedings of the National Academy of Sciences 115, 5099–5104. https://doi.org/10.1073/pnas.1801191115

Jin, X., Fiore, A., Boersma, K.F., Smedt, I.D., Valin, L., 2020. Inferring Changes in Summertime Surface Ozone–NO_x–VOC Chemistry over U.S. Urban Areas from Two Decades of Satellite and Ground-Based Observations. Environmental Science & Technology 54, 6518–6529. https://doi.org/10.1021/acs.est.9b07785

Jin, X., Fiore, A.M., Murray, L.T., Valin, L.C., Lamsal, L.N., Duncan, B., Folkert Boersma, K., De Smedt, I., Abad, G.G., Chance, K., Tonnesen, G.S., 2017. Evaluating a Space-Based Indicator of Surface Ozone-NO_x-VOC Sensitivity Over Midlatitude Source Regions and Application to Decadal Trends: Space-Based Indicator of O_3 Sensitivity. Journal of Geophysical Research: Atmospheres 122, 10,439-10,461. https://doi.org/10.1002/2017JD026720

Jung, J., Choi, Y., Wong, D.C., Nelson, D., Lee, S., 2021. Role of Sea Fog Over the Yellow Sea on Air Quality With the Direct Effect of Aerosols. Geophys Res Atmos 126. https://doi.org/10.1029/2020JD033498

Kaiser, J., Jacob, D.J., Zhu, L., Travis, K.R., Fisher, J.A., González Abad, G., Zhang, L., Zhang, X., Fried, A., Crounse, J.D., St. Clair, J.M., Wisthaler, A., 2018. High-resolution inversion of OMI formaldehyde columns to quantify isoprene emission on ecosystem-relevant scales: application to the southeast US. Atmospheric Chemistry and Physics 18, 5483–5497. https://doi.org/10.5194/acp-18-5483-2018

Kang, D., Foley, K.M., Mathur, R., Roselle, S.J., Pickering, K.E., Allen, D.J., 2019. Simulating lightning NO production in CMAQv5.2: performance evaluations. Geosci. Model Dev. 12, 4409–4424. https://doi.org/10.5194/gmd-12-4409-2019

Kang, D., Mathur, R., Pouliot, G.A., Gilliam, R.C., Wong, D.C., 2020. Significant ground-level ozone attributed to lightning-induced nitrogen oxides during summertime over the Mountain West States. npj Climate and Atmospheric Science 3, 6. https://doi.org/10.1038/s41612-020-0108-2

Kang, D., Pickering, K., 2018. Lightning NOx Emissions and the Implications for Surface Air Quality over the Contiguous United States. EM (Pittsburgh Pa) 11, 1–6.

Kitayama, K., Morino, Y., Yamaji, K., Chatani, S., 2019. Uncertainties in O3 concentrations simulated by CMAQ over Japan using four chemical mechanisms. Atmospheric Environment 198, 448–462. https://doi.org/10.1016/j.atmosenv.2018.11.003

Knowland, K.E., Ott, L.E., Duncan, B.N., Wargan, K., 2017. Stratospheric Intrusion-Influenced Ozone Air Quality Exceedances Investigated in the NASA MERRA-2 Reanalysis: SI-INFLUENCED O_3 EXCEEDANCES IN MERRA-2. Geophysical Research Letters 44, 10,691-10,701. https://doi.org/10.1002/2017GL074532

Koplitz, S., Simon, H., Henderson, B., Liljegren, J., Tonnesen, G., Whitehill, A., Wells, B., 2021. Changes in Ozone Chemical Sensitivity in the United States from 2007 to 2016. ACS Environ. Au acsenvironau.1c00029. https://doi.org/10.1021/acsenvironau.1c00029

Krotkov, N.A., Lamsal, L.N., Celarier, E.A., Swartz, W.H., Marchenko, S.V., Bucsela, E.J., Chan, K.L., Wenig, M., Zara, M., 2017. The version 3 OMI NOs standard product. Atmospheric Measurement Techniques 10, 3133–3149. https://doi.org/10.5194/amt-10-3133-2017

691 Lamsal, L.N., Krotkov, N.A., Celarier, E.A., Swartz, W.H., Pickering, K.E., Bucsela, E.J., Gleason, J.F.,
692 Martin, R.V., Philip, S., Irie, H., Cede, A., Herman, J., Weinheimer, A., Szykman, J.J., Knepp, T.N.,
693 2014. Evaluation of OMI operational standard NO2 column retrievals using in situ and surface-
694 based NO2 observations. Atmospheric Chemistry and Physics 14, 11587–11609.
695 https://doi.org/10.5194/acp-14-11587-2014
696 Lamsal, L.N., Martin, R.V., van Donkelaar, A., Steinbacher, M., Celarier, E.A., Bucsela, E., Dunlea, E.J.,
697 Pinto, J.P., 2008. Ground-level nitrogen dioxide concentrations inferred from the satellite-borne
698 Ozone Monitoring Instrument. Journal of Geophysical Research 113, D16308.
699 https://doi.org/10.1029/2007JD009235
700 Lee, H.-J., Chang, L.-S., Jaffe, D.A., Bak, J., Liu, X., Abad, G.G., Jo, H.-Y., Jo, Y.-J., Lee, J.-B., Kim, C.-H., 2021.
701 Ozone Continues to Increase in East Asia Despite Decreasing NO2: Causes and Abatements.
702 Remote Sensing 13, 2177. https://doi.org/10.3390/rs13112177
703 Levelt, P.F., van den Oord, G.H.J., Dobber, M.R., Malkki, A., Huib Visser, Johan de Vries, Stammes, P.,
704 Lundell, J.O.V., Saari, H., 2006. The ozone monitoring instrument. IEEE Transactions on
705 Geoscience and Remote Sensing 44, 1093–1101. https://doi.org/10.1109/TGRS.2006.872333
706 Li, J., Wang, Y., 2019. Inferring the anthropogenic NOx emission trend over the United States during
707 2003–2017 from satellite observations: was there a flattening of the emission trend after the
708 Great Recession? Atmospheric Chemistry and Physics 19, 15339–15352.
709 https://doi.org/10.5194/acp-19-15339-2019
710 Martin, R.V., Fiore, A.M., Van Donkelaar, A., 2004. Space-based diagnosis of surface ozone sensitivity to
711 anthropogenic emissions: SURFACE OZONE SENSITIVITY TO EMISSIONS. Geophysical Research
712 Letters 31, n/a-n/a. https://doi.org/10.1029/2004GL019416
713 Mathur, R., Xing, J., Gilliam, R., Sarwar, G., Hogrefe, C., Pleim, J., Pouliot, G., Roselle, S., Spero, T.L.,
714 Wong, D.C., Young, J., 2017. Extending the Community Multiscale Air Quality (CMAQ) modeling
715 system to hemispheric scales: overview of process considerations and initial applications.
716 Atmos. Chem. Phys. 17, 12449–12474. https://doi.org/10.5194/acp-17-12449-2017
717 Mehmood, K., Wu, Y., Wang, L., Yu, S., Li, P., Chen, X., Li, Z., Zhang, Y., Li, M., Liu, W., Wang, Y., Liu, Z.,
718 Zhu, Y., Rosenfeld, D., Seinfeld, J.H., 2020. Relative effects of open biomass burning and open
719 crop straw burning on haze formation over central and eastern China: modeling study driven by
720 constrained emissions. Atmospheric Chemistry and Physics 20, 2419–2443.
721 https://doi.org/10.5194/acp-20-2419-2020
722 Millet, D.B., Jacob, D.J., Boersma, K.F., Fu, T.-M., Kurosu, T.P., Chance, K., Heald, C.L., Guenther, A., 2008.
723 Spatial distribution of isoprene emissions from North America derived from formaldehyde
724 column measurements by the OMI satellite sensor. Journal of Geophysical Research 113,
725 D02307. https://doi.org/10.1029/2007JD008950
726 Napelenok, S., Cohan, D., Hu, Y., Russell, A., 2006. Decoupled direct 3D sensitivity analysis for particulate
727 matter (DDM-3D/PM). Atmospheric Environment 40, 6112–6121.
728 https://doi.org/10.1016/j.atmosenv.2006.05.039
729 Napelenok, S.L., Pinder, R.W., Gilliland, A.B., Martin, R.V., 2008. A method for evaluating spatially-
730 resolved NOx emissions using Kalman filter inversion, direct sensitivities, and space-based NO2
731 observations. Atmospheric Chemistry and Physics 12.
732 Orville, R.E., 2008. Development of the National Lightning Detection Network. Bulletin of the American
733 Meteorological Society 89, 180–190. https://doi.org/10.1175/BAMS-89-2-180
734 Palmer, P.I., Jacob, D.J., Fiore, A.M., Martin, R.V., Chance, K., Kurosu, T.P., 2003. Mapping isoprene
735 emissions over North America using formaldehyde column observations from space. Journal of
736 Geophysical Research: Atmospheres 108, 2002JD002153.
737 https://doi.org/10.1029/2002JD002153

738 Pleim, J.E., 2007a. A Combined Local and Nonlocal Closure Model for the Atmospheric Boundary Layer.
739 Part II: Application and Evaluation in a Mesoscale Meteorological Model. Journal of Applied
740 Meteorology and Climatology 46, 1396–1409. https://doi.org/10.1175/JAM2534.1
741 Pleim, J.E., 2007b. A Combined Local and Nonlocal Closure Model for the Atmospheric Boundary Layer.
742 Part I: Model Description and Testing. Journal of Applied Meteorology and Climatology 46,
743 1383–1395. https://doi.org/10.1175/JAM2539.1
744 Pleim, J.E., 2006. A Simple, Efficient Solution of Flux–Profile Relationships in the Atmospheric Surface
745 Layer. Journal of Applied Meteorology and Climatology 45, 341–347.
746 https://doi.org/10.1175/JAM2339.1
747 Pleim, J.E., Gilliam, R., 2009. An Indirect Data Assimilation Scheme for Deep Soil Temperature in the
748 Pleim–Xiu Land Surface Model. Journal of Applied Meteorology and Climatology 48, 1362–1376.
749 https://doi.org/10.1175/2009JAMC2053.1
750 Pleim, J.E., Xiu, A., 2003. Development of a Land Surface Model. Part II: Data Assimilation. Journal of
751 Applied Meteorology 42, 1811–1822. https://doi.org/10.1175/1520-
752 0450(2003)042<1811:DOALSM>2.0.CO;2
753 Pleim, J.E., Xiu, A., 1995. Development and testing of a surface flux and planetary boundary layer model
754 for application in mesoscale models. Journal of Applied Meteorology 34, 16–32.
755 Qu, Z., Jacob, D.J., Silvern, R.F., Shah, V., Campbell, P.C., Valin, L.C., Murray, L.T., 2021. US COVID-19
756 shutdown demonstrates importance of background NO_2 in inferring NO_x emissions from
757 satellite NO_2 observations. Geophysical Research Letters.
758 https://doi.org/10.1029/2021GL092783
759 Rodgers, C.D., 2000. Inverse Methods for Atmospheric Sounding: Theory and Practice, Series on
760 Atmospheric, Oceanic and Planetary Physics. WORLD SCIENTIFIC. https://doi.org/10.1142/3171
761 Schaub, D., Boersma, K.F., Kaiser, J.W., Weiss, A.K., Folini, D., Eskes, H.J., Buchmann, B., 2006.
762 Comparison of GOME tropospheric NO₂ columns with
763 NO₂ profiles deduced from ground-based in situ measurements. Atmos.
764 Chem. Phys. 6, 3211–3229. https://doi.org/10.5194/acp-6-3211-2006
765 Schroeder, J.R., Crawford, J.H., Fried, A., Walega, J., Weinheimer, A., Wisthaler, A., Müller, M., Mikoviny,
766 T., Chen, G., Shook, M., Blake, D.R., Tonnesen, G.S., 2017. New insights into the column CH_2O/NO_2
767 ratio as an indicator of near-surface ozone sensitivity: CH_2O/NO_2 as Indicator of O_3
768 Sensitivity. Journal of Geophysical Research: Atmospheres 122, 8885–8907.
769 https://doi.org/10.1002/2017JD026781
770 Shen, L., Jacob, D.J., Zhu, L., Zhang, Q., Zheng, B., Sulprizio, M.P., Li, K., De Smedt, I., González Abad, G.,
771 Cao, H., Fu, T., Liao, H., 2019. The 2005–2016 Trends of Formaldehyde Columns Over China
772 Observed by Satellites: Increasing Anthropogenic Emissions of Volatile Organic Compounds and
773 Decreasing Agricultural Fire Emissions. Geophysical Research Letters 46, 4468–4475.
774 https://doi.org/10.1029/2019GL082172
775 Sillman, S., 1995. The use of NO_y, H_2O_2, and HNO_3 as indicators for ozone-NO_x-hydrocarbon
776 sensitivity in urban locations. J. Geophys. Res. 100, 14175. https://doi.org/10.1029/94JD02953
777 Silvern, R.F., Jacob, D.J., Mickley, L.J., Sulprizio, M.P., Travis, K.R., Marais, E.A., Cohen, R.C., Laughner,
778 J.L., Choi, S., Joiner, J., Lamsal, L.N., 2019. Using satellite observations of tropospheric NO_2
779 columns to infer long-term trends in US NO_x emissions: the importance of accounting for the
780 free tropospheric NO_2 background. Atmospheric Chemistry and Physics 19, 8863–8878.
781 https://doi.org/10.5194/acp-19-8863-2019
782 Souri, A.H., Choi, Y., Jeon, W., Kochanski, A.K., Diao, L., Mandel, J., Bhave, P.V., Pan, S., 2017. Quantifying
783 the Impact of Biomass Burning Emissions on Major Inorganic Aerosols and Their Precursors in
784 the U.S.: Burning Impact on Inorganic Aerosols. Journal of Geophysical Research: Atmospheres
785 122, 12,020-12,041. https://doi.org/10.1002/2017JD026788

Souri, A.H., Choi, Y., Jeon, W., Li, X., Pan, S., Diao, L., Westenbarger, D.A., 2016. Constraining NOx emissions using satellite NO2 measurements during 2013 DISCOVER-AQ Texas campaign. Atmospheric Environment 131, 371–381. https://doi.org/10.1016/j.atmosenv.2016.02.020

Souri, A.H., Nowlan, C.R., González Abad, G., Zhu, L., Blake, D.R., Fried, A., Weinheimer, A.J., Wisthaler, A., Woo, J.-H., Zhang, Q., Chan Miller, C.E., Liu, X., Chance, K., 2020. An inversion of NOx and non-methane volatile organic compound (NMVOC) emissions using satellite observations during the KORUS-AQ campaign and implications for surface ozone over East Asia. Atmospheric Chemistry and Physics 20, 9837–9854. https://doi.org/10.5194/acp-20-9837-2020

Tang, W., Cohan, D.S., Lamsal, L.N., Xiao, X., Zhou, W., 2013a. Inverse modeling of Texas NOx emissions using space-based and ground-based NO2 observations. Atmospheric Chemistry and Physics 13, 11005–11018. https://doi.org/10.5194/acp-13-11005-2013

Tang, W., Cohan, D.S., Lamsal, L.N., Xiao, X., Zhou, W., 2013b. Inverse modeling of Texas NO_x emissions using space-based and ground-based NO₂ observations. Atmos. Chem. Phys. 13, 11005–11018. https://doi.org/10.5194/acp-13-11005-2013

Tarasick, D.W., Smit, H.G.J., Thompson, A.M., Morris, G.A., Witte, J.C., Davies, J., Nakano, T., Van Malderen, R., Stauffer, R.M., Johnson, B.J., Stübi, R., Oltmans, S.J., Vömel, H., 2021. Improving ECC Ozonesonde Data Quality: Assessment of Current Methods and Outstanding Issues. Earth Space Sci 8. https://doi.org/10.1029/2019EA000914

Tian, D., Cohan, D.S., Napelenok, S., Bergin, M., Hu, Y., Chang, M., Russell, A.G., 2010. Uncertainty Analysis of Ozone Formation and Response to Emission Controls Using Higher-Order Sensitivities. Journal of the Air & Waste Management Association 60, 797–804. https://doi.org/10.3155/1047-3289.60.7.797

Tonnesen, G.S., Dennis, R.L., 2000. Analysis of radical propagation efficiency to assess ozone sensitivity to hydrocarbons and NO $_x$: 2. Long-lived species as indicators of ozone concentration sensitivity. Journal of Geophysical Research: Atmospheres 105, 9227–9241. https://doi.org/10.1029/1999JD900372

Torres, O., Bhartia, P.K., Jethva, H., Ahn, C., 2018. Impact of the ozone monitoring instrument row anomaly on the long-term record of aerosol products. Atmospheric Measurement Techniques 11, 2701–2715. https://doi.org/10.5194/amt-11-2701-2018

Travis, K.R., Jacob, D.J., Fisher, J.A., Kim, P.S., Marais, E.A., Zhu, L., Yu, K., Miller, C.C., Yantosca, R.M., Sulprizio, M.P., Thompson, A.M., Wennberg, P.O., Crounse, J.D., St. Clair, J.M., Cohen, R.C., Laughner, J.L., Dibb, J.E., Hall, S.R., Ullmann, K., Wolfe, G.M., Pollack, I.B., Peischl, J., Neuman, J.A., Zhou, X., 2016. Why do models overestimate surface ozone in the Southeast United States? Atmos. Chem. Phys. 16, 13561–13577. https://doi.org/10.5194/acp-16-13561-2016

Vukovich, J.M., Eyth, A., Henderson, B., Allen, C., Beidler, J., 2018. Development of 2016 Hemispheric Emissions for CMAQ.

Wang, Y., Beirle, S., Lampel, J., Koukouli, M., De Smedt, I., Theys, N., Li, A., Wu, D., Xie, P., Liu, C., Van Roozendael, M., Stavrakou, T., Müller, J.-F., Wagner, T., 2017. Validation of OMI, GOME-2A and GOME-2B tropospheric NO2, SO2 and HCHO products using MAX-DOAS observations from 2011 to 2014 in Wuxi, China: investigation of the effects of priori profiles and aerosols on the satellite products. Atmospheric Chemistry and Physics 17, 5007–5033. https://doi.org/10.5194/acp-17-5007-2017

Wiedinmyer, C., Akagi, S.K., Yokelson, R.J., Emmons, L.K., Al-Saadi, J.A., Orlando, J.J., Soja, A.J., 2011. The Fire INventory from NCAR (FINN): a high resolution global model to estimate the emissions from open burning. Geoscientific Model Development 4, 625–641. https://doi.org/10.5194/gmd-4-625-2011

Wiedinmyer, C., Quayle, B., Geron, C., Belote, A., McKenzie, D., Zhang, X., O'Neill, S., Wynne, K.K., 2006. Estimating emissions from fires in North America for air quality modeling. Atmospheric Environment 40, 3419–3432. https://doi.org/10.1016/j.atmosenv.2006.02.010

Wiedinmyer, C., Yokelson, R.J., Gullett, B.K., 2014. Global Emissions of Trace Gases, Particulate Matter, and Hazardous Air Pollutants from Open Burning of Domestic Waste. Environmental Science & Technology 48, 9523–9530. https://doi.org/10.1021/es502250z

Xiu, A., Pleim, J.E., 2001. Development of a Land Surface Model. Part I: Application in a Mesoscale Meteorological Model. Journal of Applied Meteorology 40, 192–209. https://doi.org/10.1175/1520-0450(2001)040<0192:DOALSM>2.0.CO;2

Zhu, L., Jacob, D.J., Kim, P.S., Fisher, J.A., Yu, K., Travis, K.R., Mickley, L.J., Yantosca, R.M., Sulprizio, M.P., De Smedt, I., González Abad, G., Chance, K., Li, C., Ferrare, R., Fried, A., Hair, J.W., Hanisco, T.F., Richter, D., Jo Scarino, A., Walega, J., Weibring, P., Wolfe, G.M., 2016. Observing atmospheric formaldehyde (HCHO) from space: validation and intercomparison of six retrievals from four satellites (OMI, GOME2A, GOME2B,OMPS) with SEAC4RS aircraft observations over the southeast US. Atmospheric Chemistry and Physics 16, 13477–13490. https://doi.org/10.5194/acp-16-13477-2016

Zhu, L., Jacob, D.J., Mickley, L.J., Marais, E.A., Cohan, D.S., Yoshida, Y., Duncan, B.N., González Abad, G., Chance, K.V., 2014. Anthropogenic emissions of highly reactive volatile organic compounds in eastern Texas inferred from oversampling of satellite (OMI) measurements of HCHO columns. Environmental Research Letters 9, 114004. https://doi.org/10.1088/1748-9326/9/11/114004

Zhu, L., Mickley, L.J., Jacob, D.J., Marais, E.A., Sheng, J., Hu, L., Abad, G.G., Chance, K., 2017. Long-term (2005-2014) trends in formaldehyde (HCHO) columns across North America as seen by the OMI satellite instrument: Evidence of changing emissions of volatile organic compounds: HCHO Trend Across North America. Geophysical Research Letters 44, 7079–7086. https://doi.org/10.1002/2017GL073859

860 **Tables:**

861

862 **Table 1**. Model configurations.

WRF version 4.0	
Microphysics	Morrison double-moment scheme
Longwave and shortwave radiation	RRTMG scheme
Land surface	The Pleim-Xiu land surface model (Pleim and Xiu, 1995; Xiu and Pleim, 2001)
Surface layer	Pleim-Xiu surface layer (Pleim, 2006)
Planetary boundary layer	The ACM2 planetary boundary layer model (Pleim, 2007a, 2007b)
Cumulus parameterization	Kain-Fritsch (KF2) scheme with sub-grid cloud fraction interaction with radiation (Alapaty et al., 2012; Herwehe et al., 2014)
Four-dimensional data assimilation (FDDA)	· Indirect soil moisture and temperature nudging technique (Pleim and Gilliam, 2009; Pleim and Xiu, 2003) · A FDDA option every 6 hours above the PBL for the temperature, the water vapor mixing ratio, and wind components (magnitude of 10^{-5}) (Hogrefe et al., 2015)
Initial and boundary conditions for meteorology	National Centers for Environmental Prediction (NCEP) North American Reginal Reanalysis (NARR) data
CMAQ-DDM version 5.2	
Chemical mechanism	CB6 and AERO6
Horizontal advection	YAMO
Vertical advection	WRF omega formula
Horizontal diffusion	Multiscale
Vertical diffusion	ACM2
Initial and boundary conditions for chemistry	The CMAQ model version 5.3 with the in-line dust module covering the entire northern hemisphere in conjunction with scaling for gaseous species based on the comparison with satellite measurements

863

864

865

866

867

868

869

Table 2. Model performance for the simulation of meteorological variables (i.e., air temperature, U and V wind components) compared to the AQS measurements. We considered only stations with valid data for more than 50% of the study period. (RMSE: root-mean-square error, CORR: correlation, IOA: the index of agreement, MB: mean bias).

	Variables	Number of stations	Mean		RMSE	CORR	IOA	MB
			OBS	MOD				
2011 JJA	Air Temp ([ºC])	573	23.87	25.12	3.57	0.87	0.90	1.29
	U wind ([m/s])	552	0.21	0.59	2.12	0.50	0.63	0.38
	V wind ([m/s])	552	0.58	0.61	2.13	0.46	0.61	0.03
2014 JJA	Air Temp ([ºC])	558	23.18	24.26	3.23	0.86	0.89	1.08
	U wind ([m/s])	620	0.21	0.56	2.04	0.50	0.63	0.34
	V wind ([m/s])	620	0.45	0.40	2.20	0.50	0.62	-0.05
2017 JJA	Air Temp ([ºC])	600	24.10	24.95	3.15	0.87	0.90	0.84
	U wind ([m/s])	691	0.26	0.61	2.00	0.48	0.62	0.36
	V wind ([m/s])	691	0.31	0.32	2.16	0.49	0.62	0.01

886 **Figures:**

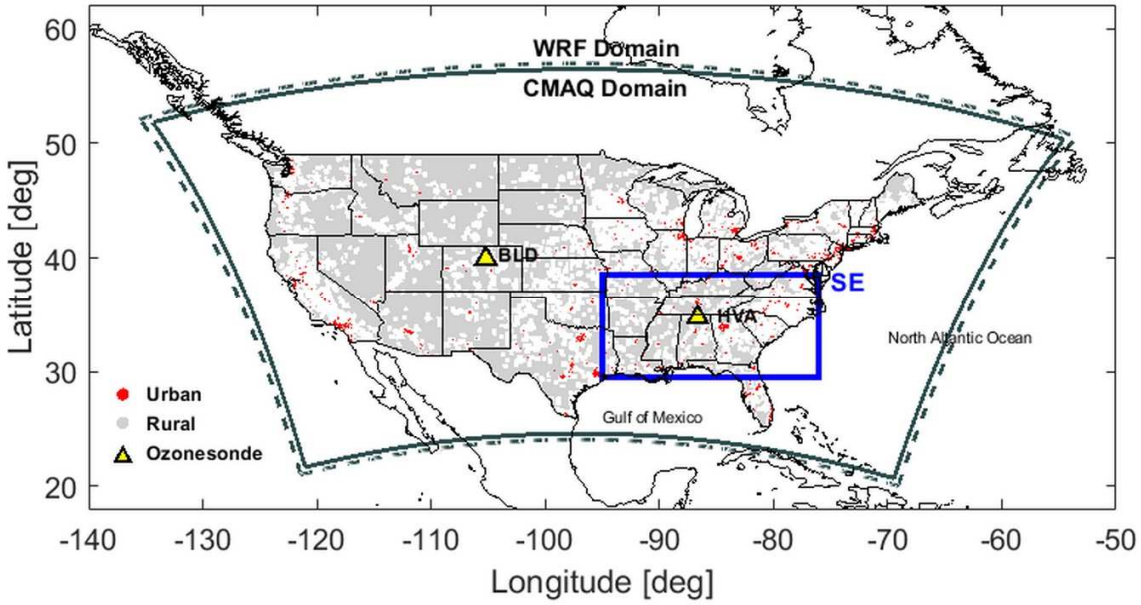

887

888 **Figure 1.** Map of the study domain and definition of urban (red) and rural (gray) regions over
889 the CONUS. The yellow triangle symbols represent the location of ozonesonde stations (BLD:
890 Boulder, HVA: Huntsville).

891

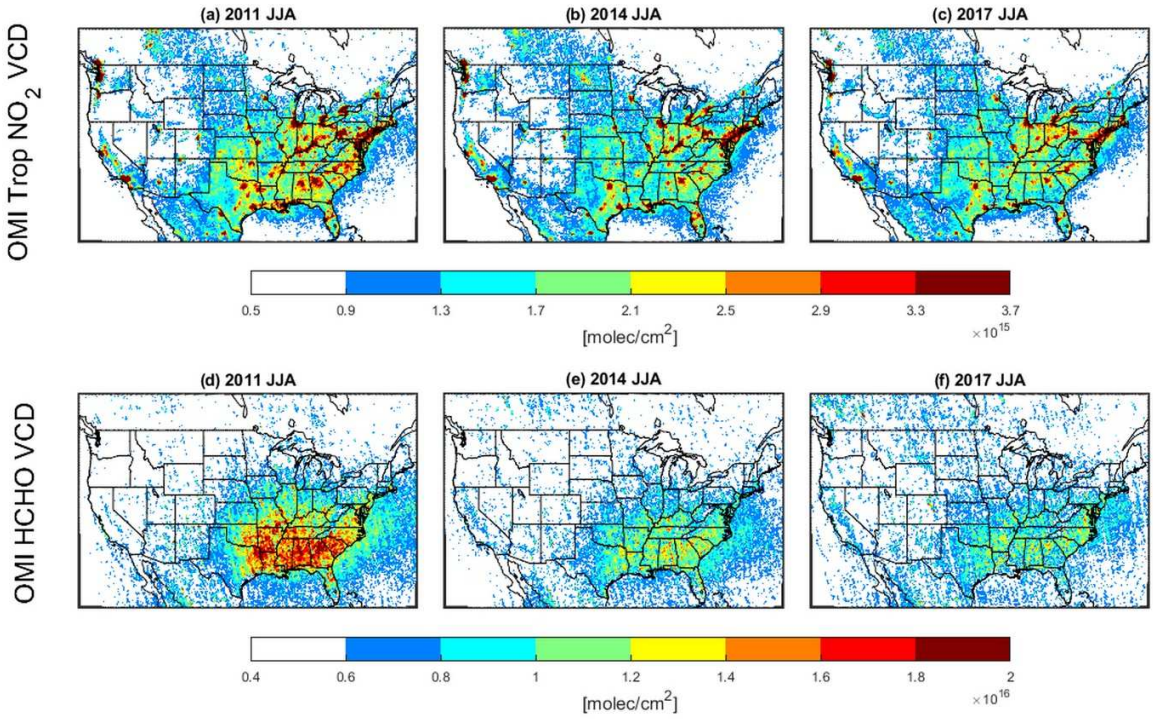

892

893 **Figure 2.** Spatial distribution of (a to c) the OMI tropospheric NO_2 vertical column density and
894 (d to f) the OMI HCHO vertical column density in the summers (June - August) of 2011, 2014,
895 and 2017.

896

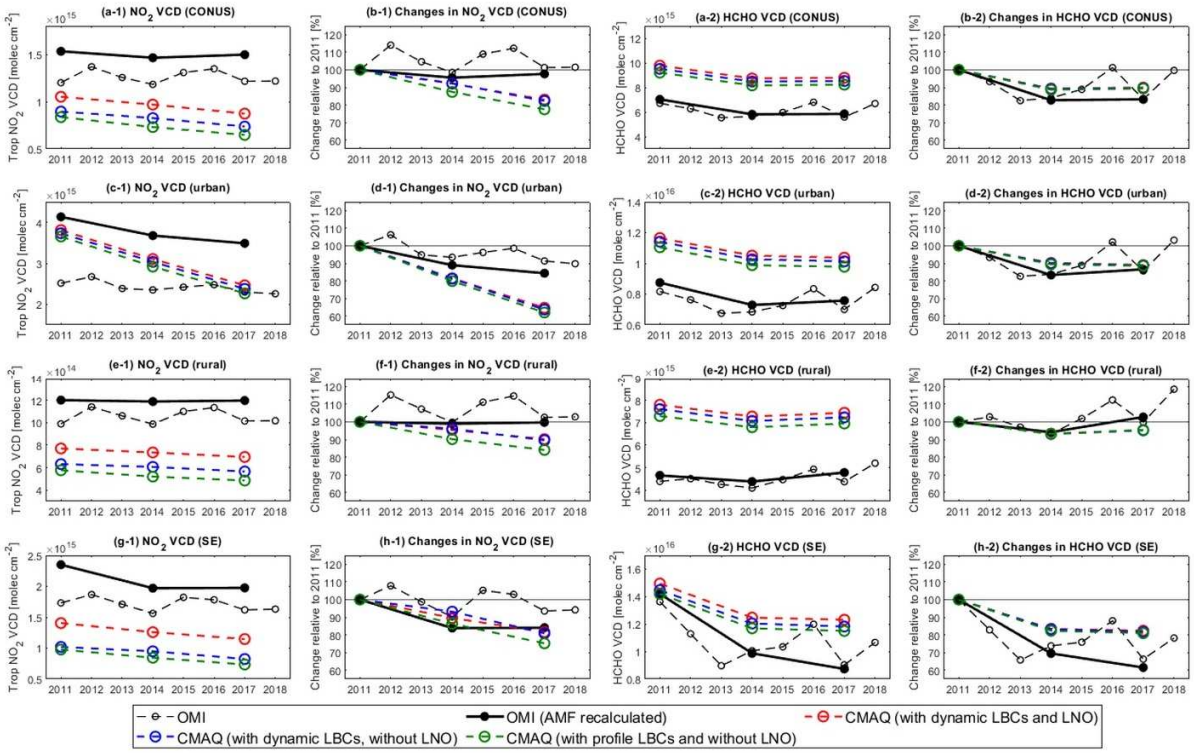

Figure 3. The long-term trend in summertime averaged tropospheric (a-1 to h-1) NO_2 and (a-2 to h-2) HCHO columns observed by the OMI satellite (2011 – 2018) and simulated by the CMAQ model (2011, 2014, and 2017), and their relative changes in the CONUS and urban, rural, and southeastern U.S. regions (shown in Figure 1). CMAQ simulations were conducted with the prior emission and three background setups (with dynamic lateral boundary conditions and lightning emissions (LNO), with dynamic lateral boundary conditions and without lightning emissions, and with profile lateral boundary conditions and without lightning emissions).

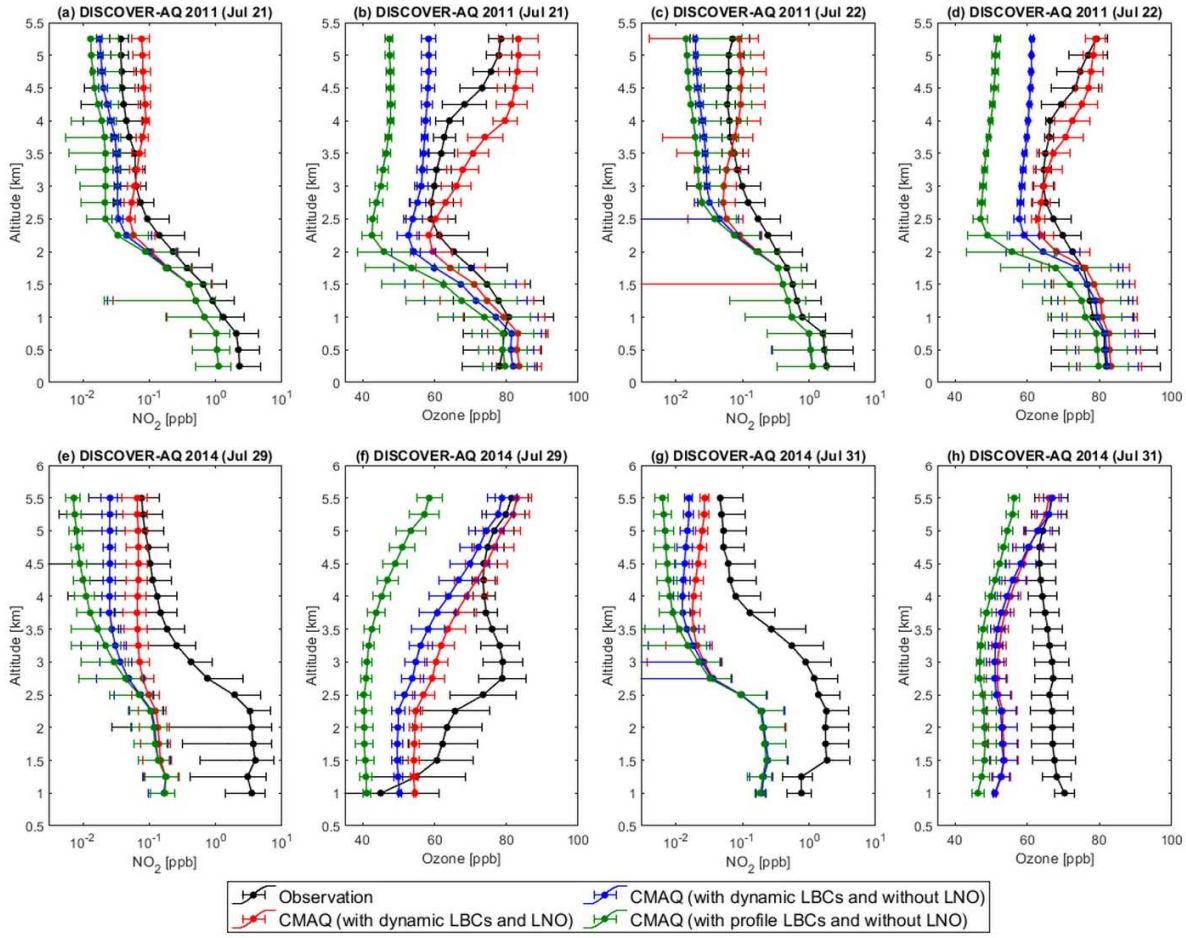

906

907 **Figure 4.** Comparisons of the vertical distribution of ozone and nitrogen dioxide (NO_2)
908 concentrations measured during the DISCOVER-AQ (a to d) 2011 (July 21 and 22) and (e to h)
909 2014 (July 29 and 31) campaigns and modeled concentrations with prior emissions and three
910 background setups (i.e., with dynamic lateral boundary conditions and LNO emissions, with
911 dynamic lateral boundary conditions and without LNO emissions, and with profile lateral
912 boundary conditions and without LNO emissions). Error bars represent the standard deviation.

913

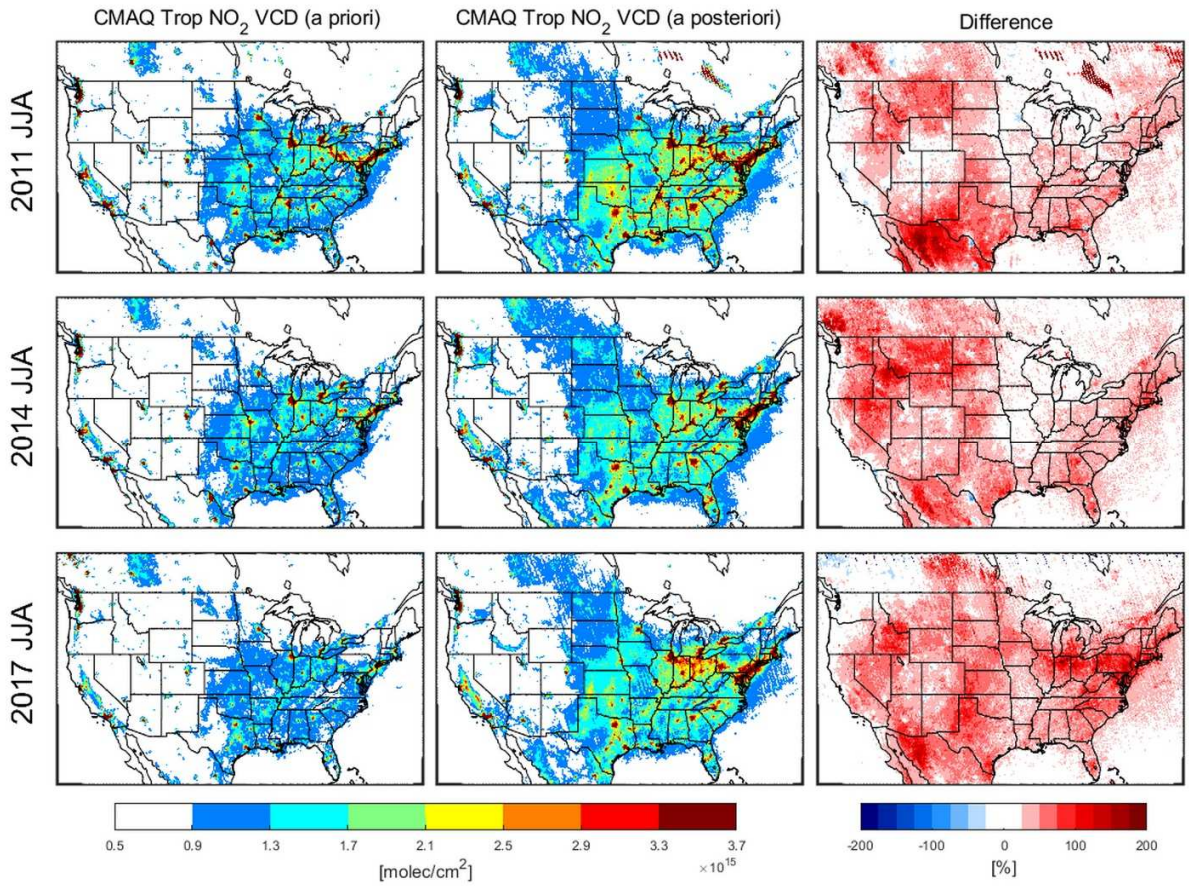

914

915 **Figure 5.** Spatial distribution of the modeled NO_2 vertical column densities with prior and
916 posterior emissions and their relative differences with respect to the modeled column density
917 with prior emissions in the summers (June - August) of 2011, 2014, and 2017.

918

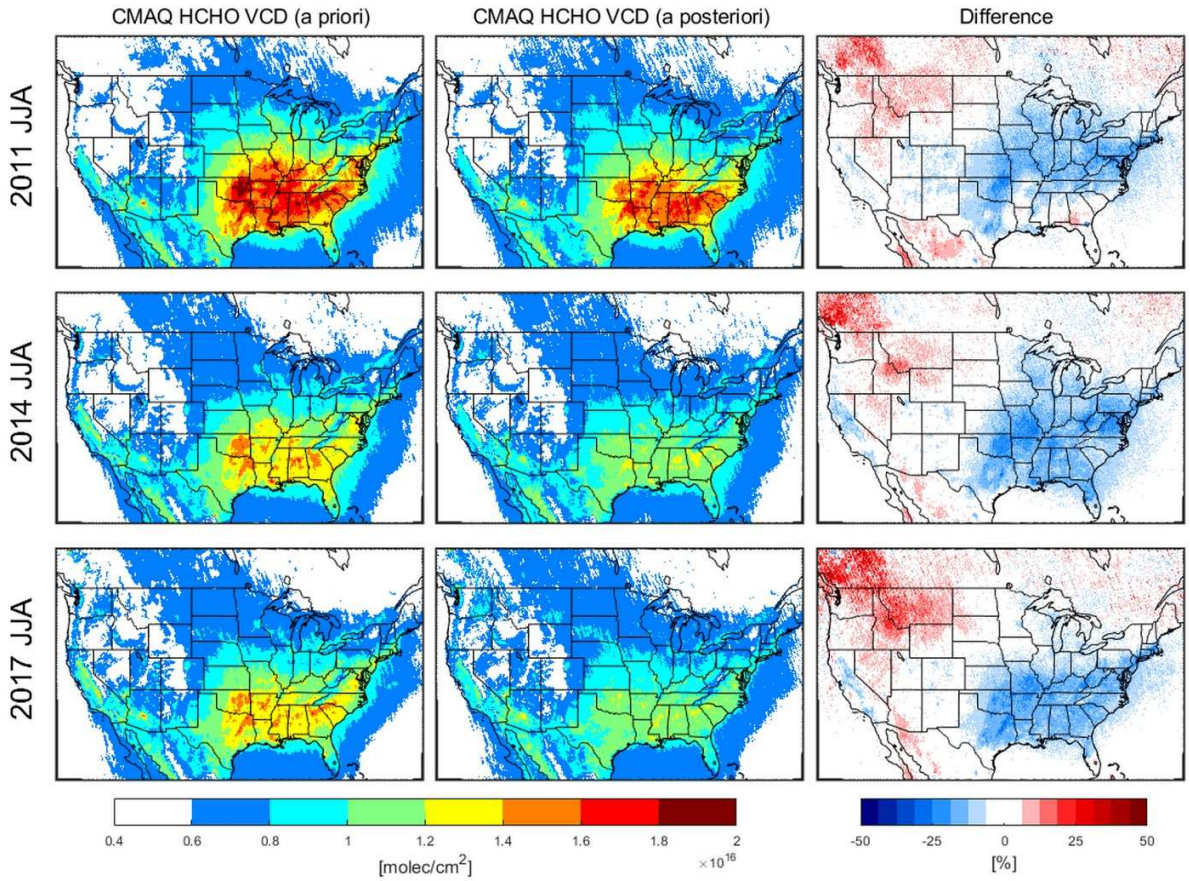

Figure 6. Spatial distribution of the modeled HCHO vertical column densities with prior and posterior emissions, and their relative differences with respect to the modeled column density with prior emissions in the summers (June - August) 2011, 2014, and 2017.

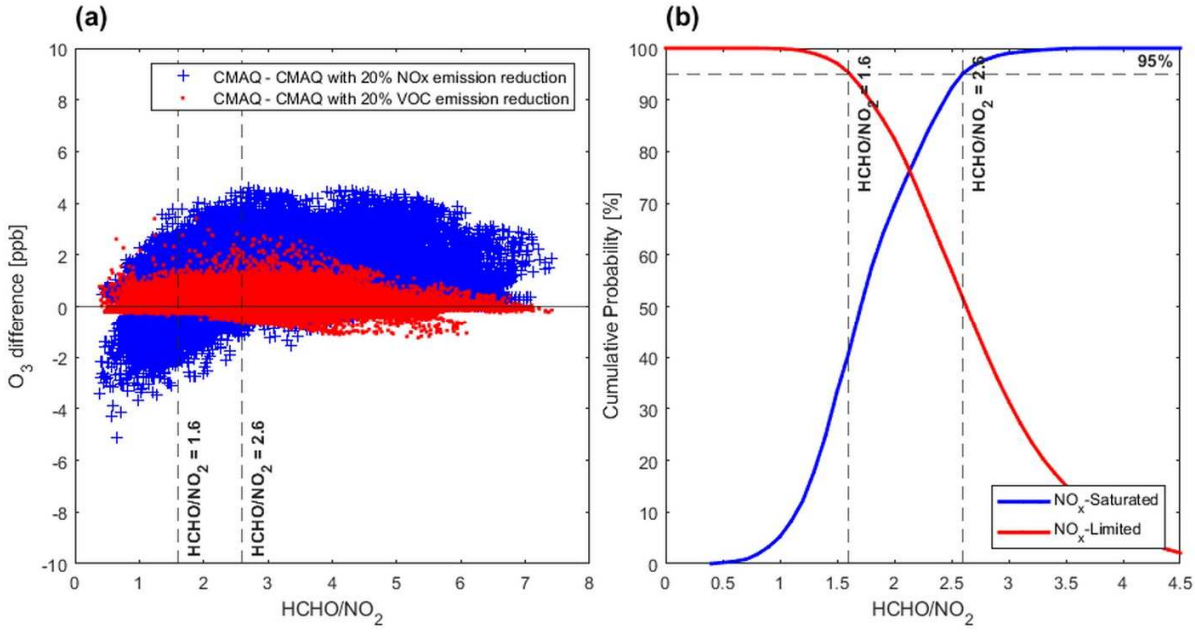

924

925 **Figure 7**. (a) Difference between the surface ozone concentrations of the baseline model output
926 (with posterior emissions) and emission reduction cases (20% reduction in NO_x and NMVOCs
927 emissions) with the ratio of the modeled HCHO column to the NO_2 column in the summer of
928 2011; (b) the cumulative probability of NO_x-limited and NO_x-saturated conditions with respect to
929 the ratio of the modeled HCHO column to the NO_2 column following Jin et al. (2017). Both are
930 estimated from daily averaged $HCHO/NO_2$ values and surface O_3 concentrations for the revisit
931 time of the OMI satellite (13:00-14:00 LST) over polluted regions (modeled NO_2 column > $1 \times$
932 10^{15} molecules cm^{-2}).

933

934

935

936

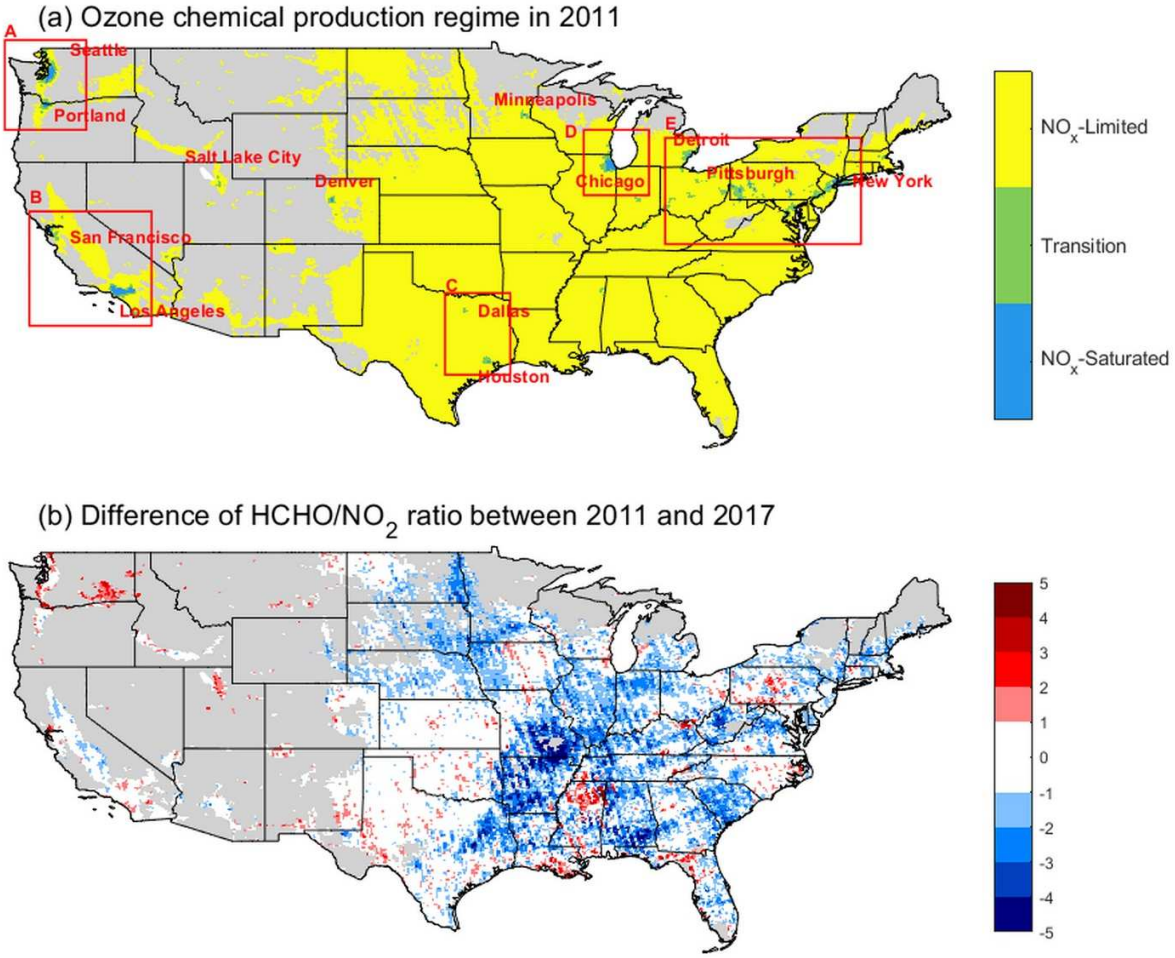

937

938 **Figure 8.** (a) Spatial distribution of the ozone chemical production regime over the CONUS for
939 the year 2011. (b) The difference between the HCHO/NO_2 ratios of 2011 and 2017. Gray areas
940 represent tropospheric NO_2 column densities that are less than 1×10^{15} molecules cm^{-2}.

941

942

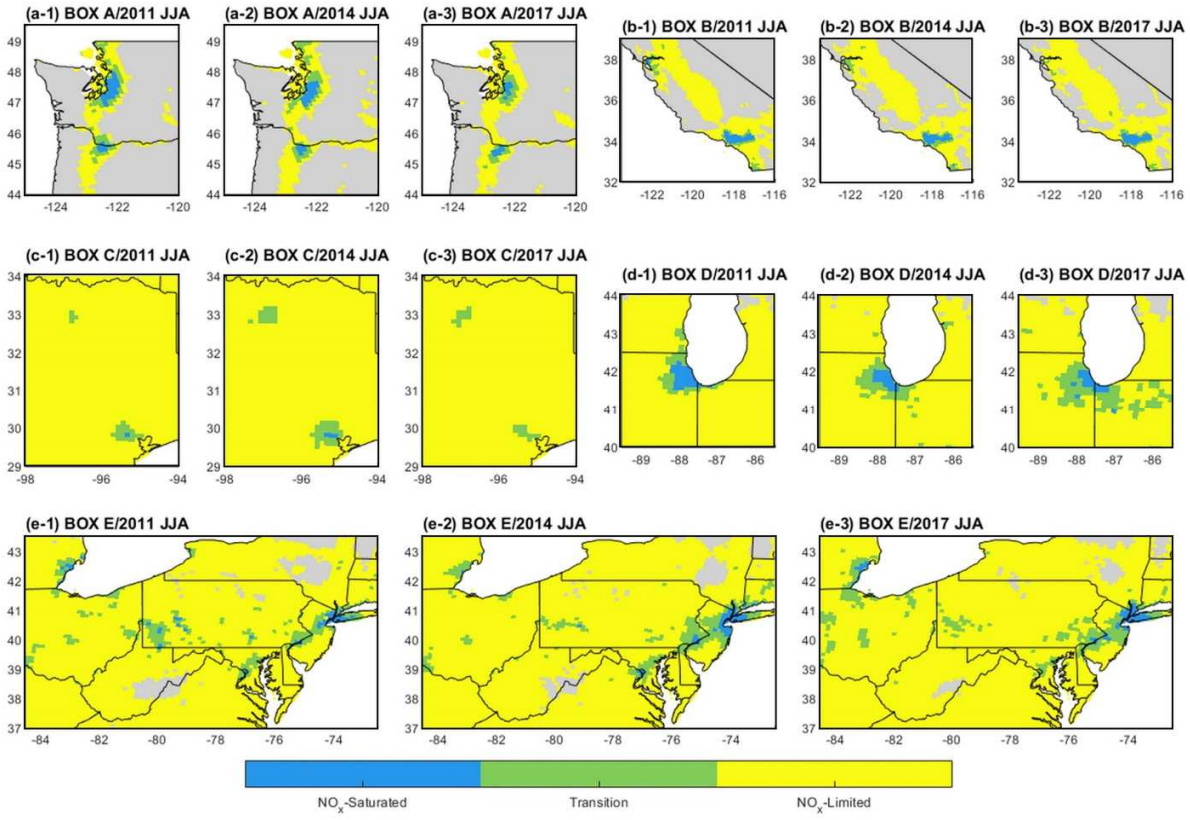

943

944 **Figure 9.** Changes in the ozone production regime over the 5 boxes denoted in Figure 8.

945

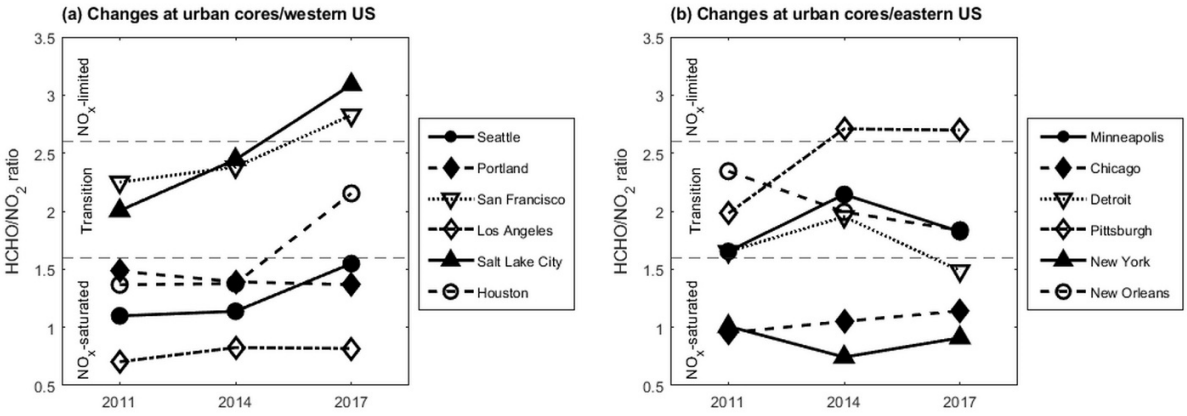

946

947 **Figure 10.** Changes in the HCHO/NO_2 ratio from urban cores for 12 main cities over (a) the
948 western U.S. (Seattle, Portland, San Francisco, Los Angeles, Salt Lake City, and Houston), and
949 (b) the eastern U.S. (Minneapolis, Chicago, Detroit, Pittsburgh, New York, and New Orleans).

950

951

952

953

954

955

956